

23 946889



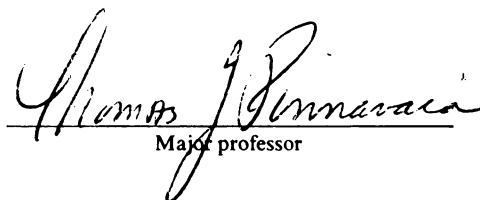
This is to certify that the
dissertation entitled
Transverse Layer Rigidity in Vermiculite
Pillared by Mixed Alkylammonium Ions

presented by

Hyungrok Kim

has been accepted towards fulfillment
of the requirements for

Ph.D. Chemistry
degree in


Major professor

Date July 21 1989

**PLACE IN RETURN BOX to remove this checkout from your record.
TO AVOID FINES return on or before date due.**

DATE DUE	DATE DUE	DATE DUE
_____	_____	_____
_____	_____	_____
_____	_____	_____
_____	_____	_____
_____	_____	_____
_____	_____	_____
_____	_____	_____

MSU Is An Affirmative Action/Equal Opportunity Institution

TRANSVERSE LAYER RIGIDITY IN VERMICULITE PILLARED BY
MIXED ALKYLAMMONIUM IONS

By
Hyungrok Kim

A DISSERTATION

Submitted to
Michigan State University
in partial fulfillment of the requirements
for the degree of

DOCTOR OF PHILOSOPHY

Department of Chemistry

1989

6040263

ABSTRACT

TRANSVERSE LAYER RIGIDITY IN VERMICULITE PILLARED BY MIXED ALKYLAMMONIUM IONS

By

Hyungrok Kim

The mixed alkylammonium ion pillared clay system $[(CH_3)_4N^+]_x[(CH_3)_3NH^+]_{1-x}$ -vermiculites ($x=0-0.96$) has been shown to be suitable for quantitatively describing the transverse layer rigidity of the host clay layers by observing the relationship between gallery height and the fraction of pillaring $(CH_3)_4N^+$ ions occupying the gallery surfaces.

The mixed ion $[(CH_3)_4N^+]_x[(CH_3)_3NH^+]_{1-x}$ -vermiculites were prepared by the partial exchange of $(CH_3)_3NH^+$ ions in $[(CH_3)_3NH^+]$ -vermiculite with the appropriate amounts of $(CH_3)_4N^+$ ions.

Very poor agreement was obtained between the X-ray diffraction peak positions of the observed and the calculated 001 reflections based on the Hendricks-Teller and Reynolds models for ion segregation. However, the observed patterns were in good agreement with the Bragg model for uniform ion mixing within the galleries. Also, a one-dimensional Patterson synthesis of the mixed ion system showed vector distributions corresponding to a unique d-

spacing. In addition, the experimentally observed x dependence of the normalized d -spacings ($d_n(x) = (d(x) - d(0)) / (d(1) - d(0))$) of the $[(CH_3)_4N^+]_x[(CH_3)_3NH^+]_{1-x}$ -vermiculites deviated strongly from the expected behavior for an ion-segregated system. Thus, the diffraction data are consistent with the random distribution of both ions within each gallery, as opposed to ion-demixed intercalates in which the two ions occupy separate galleries.

A rapid rise in $d_n(x)$ with increasing x was observed near the threshold value of $x_t = 0.2$ and the maximum possible $d_n(x)$ value of 1.0 was observed near an x value of 0.6. A model which related $d_n(x)$ to the layer rigidity parameter p , the binding energy difference between the gallery sites and the non-gallery(defect) sites, and the ratio of the two sites yielded an excellent fit to the experimental $d_n(x)$. A layer rigidity parameter $p=8$, a binding energy difference of 2.5 Kcal/mole, and the defect site ratio of 33 % were determined for the vermiculite host layers.

ACKNOWLEDGEMENTS

I would like to express sincere thanks to Professor T. J. Pinnavaia for his great personality, guidances, and encouragement throughout the short science journey.

I also want to express thanks to my whole family, specially to Hyoran for their patience and love.

The kindness from the people of U. S. A. and the financial supports from NSF are very appreciated.

TABLE OF CONTENTS

	Page
LIST OF TABLES	vii
LIST OF FIGURES	viii
I. INTRODUCTION	1
I-1. Structure and Properties of 2:1 Type Clay Minerals	1
I-2. Pillared Clays as Two-dimensional Microporous Material	6
I-3. Transverse Layer Rigidity and Access in Pillared Clays	10
I-4. Approach to Characterizing the Transverse Rigidity of Clay Layers	12
I-5. Defining the Mixed-Ion Clay System	17
II. EXPERIMENTAL	18
II-1. Materials	18
II-2. Synthesis	18
II-2-1. $[(CH_3)_3NH^+]$ -Vermiculite	18
II-2-2. $[(CH_3)_4N^+]$ -Vermiculite	19
II-2-3. Mixed Ion $[(CH_3)_4N^+]_x[(CH_3)_3NH^+]_{1-x}$ Vermiculites	20
II-3. Characterization	20
II-3-1. Exchange Ion Compositions of $[(CH_3)_4N^+]_x[(CH_3)_3NH^+]_{1-x}$ - Vermiculites	20
II-3-2. X-ray Diffraction Patterns	21
II-3-3. Modeling X-ray Diffraction Patterns	22
II-3-4. MacEwan Direct Fourier Transform of XRD Patterns	22

	Page
II-3-5. Infrared Spectroscopy	23
II-3-6. Raman Spectroscopy	24
II-3-7. Chemical Analysis	24
II-4. Modeling the Composition Dependence of Gallery Height for $[(CH_3)_4N^+]_x$ $[(CH_3)_3NH^+]_{1-x}$ -Vermiculite	25
III. RESULTS	27
III-1. Synthesis	27
III-2. X-ray Diffraction	31
III-3. Generation of $d_n(x)$ vs x Plots for Mixed Ion Monolayer Model	44
III-4. Infrared and Raman Spectroscopies of Mixed $[(CH_3)_4N^+]_x[(CH_3)_3NH^+]_{1-x}$ -Vermiculites	46
IV. DISCUSSION	53
V. CONCLUSIONS	66
APPENDIX I	67
APPENDIX II	73
APPENDIX III	76
REFERENCES	78

LIST OF TABLES

Table		Page
1	Idealized Structural Formulae for Representative 2:1 Phyllosilicates. In each formula the bracket and the parentheses define metal ions in octahedral and tetrahedral sites, respectively	5
2	Compositions of Representative $[\text{Me}_4\text{N}^+]_x[\text{Me}_3\text{NH}^+]_{1-x}^-$ Vermiculites Obtained by Reaction of $[\text{Me}_3\text{NH}^+]^-$ Vermiculite with Aqueous Me_4NCl	32

LIST OF FIGURES

Figure		Page
1	<p>Schematic illustration of the tetrahedral and octahedral sheets in a 2:1 layered silicate layer.</p> <p>open circle: oxygen shade circle: hydroxyl group small closed circle: tetrahedral site cation Si,Al large closed circle: octahedral site cation Al,Mg, Fe, Li, vacant</p>	2
2	<p>(a) The idealized Kagome net defined by the 3-membered and 6-membered oxygen rings in the basal surfaces of a 2:1 layer lattice silicate. The primitive cell (---) and lattice parameter, $a=5.34 \text{ \AA}$ of an undistorted lattice are also shown.</p> <p>(b) Distortions in the Kagome net due to in-plane rotations of the Si(Al)O_4 tetrahedra</p>	4
3	<p>(a) Schematic representation of the pillaring of clay. \oplus and P^+ are simple and robust cations, respectively.</p> <p>(b) Typical types of pillaring agents: tetraalkylammonium; bicyclic amine cations; polyhydroxyl or oxo cations; metal chelates</p>	8
4	<p>Schematic representation of the layers of a pillared clay assuming</p> <p>(a) Rigid layers</p> <p>(b) Flexible layers</p>	11
5	<p>(a) The concept of probing layer distortions by increasing lateral pillar separation.</p> <p>(b) The concept of probing layer distortions by mixing large and small ions in a mixed ion clay</p>	13
6	<p>Schematic representation of the expected relationship between d_n and x in $[\text{A}]_x[\text{B}]_{1-x} - \text{Y}$.</p> <p>(a) Infinitely rigid layers</p> <p>(b) Infinitely flexible layers</p>	15
7	<p>Plots for comparing of ion exchange reactivity of powdered Mg^{2+}-vermiculite with $(\text{CH}_3)_3\text{NH}^+$, and $(\text{CH}_3)_4\text{N}^+$ in the absence of EDTA anion. After each 24 hour reaction period, the ion</p>	

- exchange solution was replenished with a fresh solution containing an excess of alkylammonium ion. The ratio of alkylammonium ion : Mg^{2+} was 54:1 for the first four reaction periods, and 108:1 for the last two reaction periods. 29
- 8 X-ray diffraction patterns for $(CH_3)_3NH^+$ -vermiculite as (a) freshly prepared wet gel, (b) a film dried 1 hr. in air, and (c) an oriented film dried 1 hr at 100 °C. All diffraction patterns were recorded under equivalent conditions of x-ray exposure 33
- 9 X-ray diffraction patterns for oriented film samples of representative $[(CH_3)_4N^+]_x[(CH_3)_3NH^+]_{1-x}$ -vermiculites heated at 100 °C 35
- 10 Comparison of the observed and calculated xrd pattern for homoionic $(CH_3)_3NH^+$ -vermiculite 36
- 11 Comparison of the observed and calculated xrd pattern for homoionic $(CH_3)_4N^+$ -vermiculite 37
- 12 Comparisons of observed and calculated xrd patterns based on three models for $[(CH_3)_4N^+]_{0.63}[(CH_3)_3NH^+]_{0.37}$ - vermiculite
BRG: Bragg model. H-T: Hendricks-Teller model
REY: Reynolds model, EXP: Experimental pattern 39
- 13 Direct MacEwan transform of xrd pattern of $[(CH_3)_4N^+]_{0.63}[(CH_3)_3NH^+]_{0.37}$ - vermiculite 40
- 14 Representative Q vs l plots for $[(CH_3)_4N^+]_x[(CH_3)_3NH^+]_{1-x}$ -vermiculites. The broken lines are the linear least squares fit to the data points 42
- 15 The composition dependence of the normalized basal spacings for $[(CH_3)_4N^+]_x[(CH_3)_3NH^+]_{1-x}$ -vermiculites. Solid line is the least square fit to the data using Equation 7 of the text with the following parameter set: $p=8.0$; $f=0.5$; $\Delta/kT=4.3$ 43
- 16 The composition dependence of the normalized basal spacing for ion segregation in $[(CH_3)_4N^+]_x[(CH_3)_3NH^+]_{1-x}$ -vermiculites based on the Reynolds model. The basal spacings were calculated from least square regression of the first six 001 reflections 45

- 17 Monolayer triangular lattice simulations (dotted lines) of $d_n(x)$ for idealized $[A]_x[B]_{1-x}$ -vermiculites for several different values of the healing length, λ , and the layer rigidity parameter, p . The solid lines are from Equation 4 of the text with (1) $p=1, \lambda=0$; (2) $p=7, \lambda=a_0$; (3) $p=13, \lambda=\sqrt{3} a_0$; $p=\infty, \lambda=\infty$. Inset: the triangular lattice defined by the spherical A and B pillaring cations. The expanded region represents the distortion which occurs in the host layer when A replaced B and $\lambda=a_0$. In this latter case, the number of expanded sites is $p=n+1=7$ where n is the number of nearest neighbors..... 47
- 18 IR spectra of $(CH_3)_3NH^+$ -vermiculite with different incident beam angles. Note the change in relative peak intensity of the N^+-H stretching at 2730 cm^{-1} relative to other angle-independent peaks 48
- 19 IR spectra of $[(CH_3)_4N^+]_{0.54}[(CH_3)_3NH^+]_{0.46}$ -vermiculite for different incident beam angles. Note the change in relative peak intensity of the N^+-H stretching at 2730 cm^{-1} relative to other angle-independent peaks 49
- 20 Low frequency Raman spectra of $[(CH_3)_4N^+]_x[(CH_3)_3NH^+]_{1-x}$ -vermiculites. The insert identifies the eigenvector of the vibration 51
- 21 X-dependence of the torsional mode frequency for $[(CH_3)_4N^+]_x[(CH_3)_3NH^+]_{1-x}$ -vermiculites. The error bar indicates the uncertainty in the frequency measurements 52
- 22 Schematic illustration of possible non-gallery defect sites for exchange ions on the basal surfaces (designated x) which do not contribute to the 001 basal spacing
 (a).Surfaces at twisted layer-planar layer interfaces,
 (b).Surfaces of bifurcated layers,
 (c).Surfaces of internal and external ledges and crevasses formed by layer termination,
 (d).Surfaces of layer edge-layer face interfaces.
 Defects (a)-(d) are in addition to non-gallery binding sites at layer edges(e) 61

- 23 Plot of x the dependence of gallery ion composition (x_g) on the total $(\text{CH}_3)_4\text{N}^+$ composition (x) for $[(\text{CH}_3)_4\text{NH}^+]_x[(\text{CH}_3)_3\text{NH}^+]_{1-x}$ -vermiculites. The two binding site model assumes $p=8$, $f=0.5$, and $\Delta/kT=4.3$ 63
- 24 2θ dependence of the LP factor, squared structure factor, interference function, and intensity in the xrd pattern calculation of $(\text{CH}_3)_3\text{NH}^+$ -vermiculite 70
- 25 Comparison of observed and calculated xrd patterns for $[(\text{CH}_3)_4\text{N}^+]_{0.63}[(\text{CH}_3)_3\text{NH}^+]_{0.37}$ - vermiculite using $x_g=0.45$
 H-T : Hendricks-Teller calculation
 EXP.: Observed xrd pattern 74
- 26 Comparison of observed and calculated xrd patterns for $[(\text{CH}_3)_4\text{N}^+]_{0.63}[(\text{CH}_3)_3\text{NH}^+]_{0.37}$ - vermiculite using $x_g=0.45$
 REY : Reynolds calculation
 EXP : Observed xrd pattern 75

I. INTRODUCTION

I-1. Structure and Properties of 2:1 Type Clay Minerals

Layered alumino-silicates minerals, generally known as clay minerals, have different forms that vary from amorphous powders to single crystals. They also show broad variations in chemical and physical properties.^{1,2} Even among clays with almost same layer lattice structures where the basic sub-layer building blocks are almost identical, their properties can vary greatly. These two-dimensional layer structures consist of sheets of MO_4 tetrahedra and a sheet of $\text{M}'\text{O}_6$ octahedra where M is most commonly Si^{4+} and, occasionally, Al^{3+} or Fe^{3+} , and M' is Al^{3+} , Fe^{3+} , Mg^{2+} , Li^{+} or a vacancy. Also, some of the oxygens of the $\text{M}'\text{O}_6$ are replaced by hydroxy groups. Thus, the various clay layers may be considered as condensed products of the two different kinds of sheets.³

The 2:1 layer lattice structures of interest in this research contain two tetrahedral sheets fused to a central octahedral sheet.⁴ Fig. 1 illustrates the idealized 2:1 structure along with the interlayer cations. For simplicity, metal cations in both the tetrahedral sites and the octahedral sites of layers are shown using solid circles. The surfaces of the unit layer are composed of basal oxygen

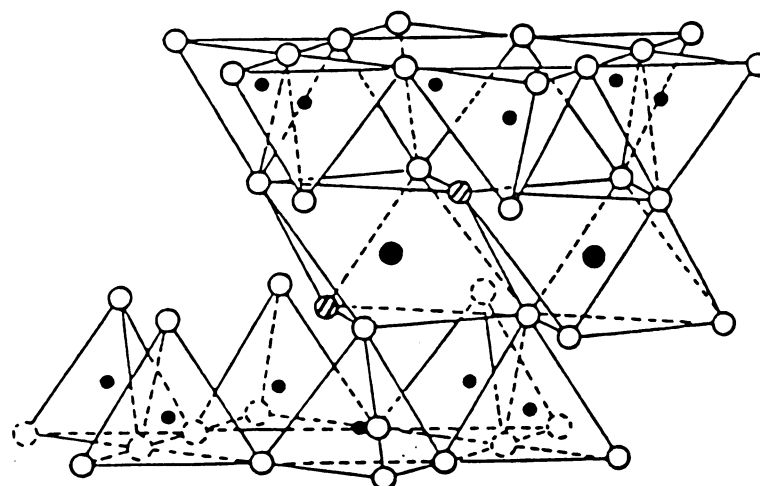
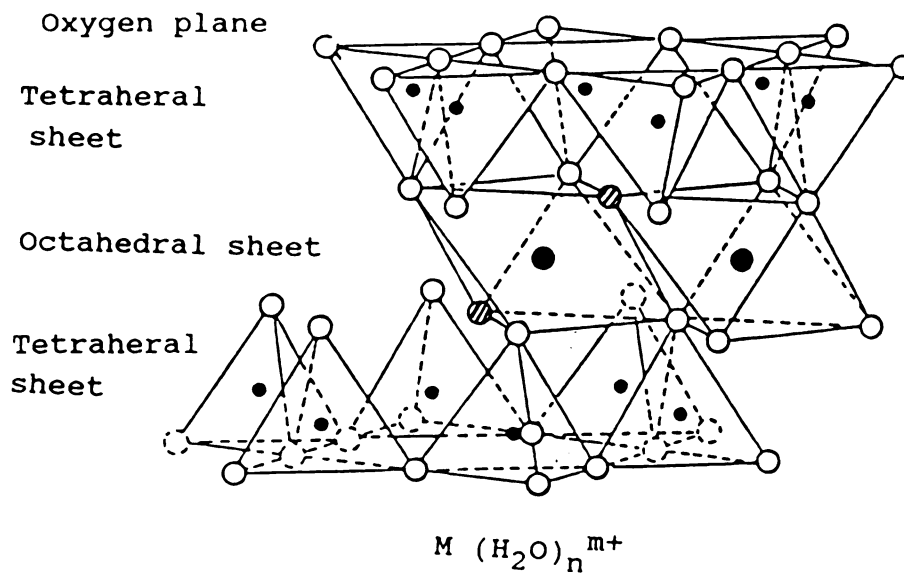
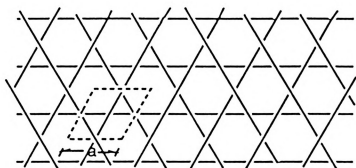


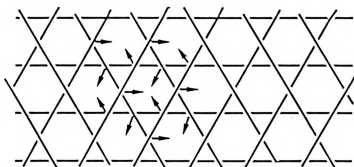
Fig. 1 Schematic illustration of the tetrahedral and octahedral sheets in a 2:1 layered silicate layer.
 open circle: oxygen shade circle: hydroxyl group
 small closed circle: tetrahedral site cation Si, Al
 large closed circle: octahedral site cation Al, Mg, Fe, Li, vacant

planes which define a Kagome net containing 3-membered and 6-membered oxygen rings. This net is described Fig. 2(a). Ideally, 6-oxygen rings form sites of hexagonal symmetry. In a real layer, tetrahedral rotations occur around the Si(Al)-O bonds perpendicular to the basal plane, because of a misfit between the b parameters of the individual tetrahedral and octahedral sheets. The directions of the tetrahedral Si(Al)O₄ rotations are indicated by the arrows in Fig. 2(b). The rotation of the tetrahedral sites changes the cavity symmetry from hexagonal toward trigonal,¹ but the triangular lattice symmetry which is defined by the centers of 6-membered oxygen cavities is not affected by the rotation. The thickness of a layer is about 9.6 Å.

In the unit cell of 2:1-type clay minerals, twenty oxygen atoms and four hydroxy groups form a 44 e⁻ anion framework which defines six octahedral sites and eight tetrahedral sites for occupancy by layer cations, along with four 6-membered oxygen cavities.¹ The idealized chemical formulae of various kinds of 2:1-type clay minerals are summarized in Table 1. The terms "dioctahedral" and "trioctahedral" mean that two-thirds and three-thirds of the octahedral sites are occupied by metal cations, respectively. As shown in Table 1, a large portion of 2:1 type clay layers are negatively charged. These negative charges are balanced by interlayer cations. Depending on the amount of layer charge, 2:1-type clay minerals can be divided into 5 groups: the talc-pyrophyllite, smectite,



(a)



(b)

- Fig. 2 (a) The idealized Kagome net defined by the 3-membered and 6-membered oxygen rings in the basal surfaces of a 2:1 layer lattice silicate. The primitive cell (---) and lattice parameter, $a=5.34 \text{ \AA}$ of an undistorted lattice are also shown.
- (b) Distortions in the Kagome net due to in-plane rotations of the $\text{Si(Al)}\text{O}_4$ tetrahedra.

Table 1. Idealized structural formulae for representative 2:1 phyllosilicates. In each formula the bracket and the parentheses define metal ions in octahedral and tetrahedral sites, respectively.

Mineral group	Diocahedral	Triocahedral
Phyrophyllite - Talc	Phyrophyllite: $[Al_{4-0}](Si_{8-0})O_{20}(OH)_4$	Talc: $[Mg_{6-0}](Si_{8-0})O_{20}(OH)_4$
Smectite ($x=0.4-1.2$)	Montmorillonite: $M_{x/n}^{n+}yH_2O[Al_{4-x}Mg_x](Si_8)O_{20}(OH)_4$	Hectorite: $M_{x/n}^{n+}yH_2O[Mg_{6-x}Li_x](Si_8)O_{20}(OH)_4$
	Beidellite: $M_{x/n}^{n+}yH_2O[Al_4](Si_{8-x}Al_x)O_{20}(OH)_4$	Saponite: $M_{x/n}^{n+}yH_2O[Mg_6](Si_{8-x}Al_x)O_{20}(OH)_4$
Vermiculite ($x=1.2-1.8$)		Vermiculite $Mg_{x/n}^{n+}yH_2O[Mg_6](Si_{8-x}Al_x)O_{20}(OH)_4$
Mica	Muscovite: $K_2^+[Al_4](Si_6 Al_2)O_{20}(OH)_4$	Phlogopite : $K_2^+[Mg_6](Si_6 Al_2)O_{20}(OH)_4$
Brittle Mica	Margarite : $Ca_2^{2+}[Al_4](Si_4 Al_4)O_{20}(OH)_4$	Clintonite : $Ca_2^{2+}[Mg_4 Al_2](Si_2 Al_6)O_{20}(OH)_4$

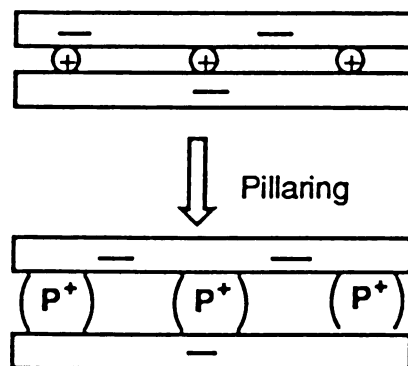
vermiculite, mica, and brittle mica groups. In the talc-pyrophyllite group, the layers are electrically neutral and coupled through van der Waals forces.⁵ In the other extreme, mica and brittle mica minerals possess 2 e⁻ and 4 e⁻ layer charges per O₂₀(OH)₄ unit, respectively, and the counter cations, usually K⁺ and Ca²⁺, are tightly bound in the ditrigonal oxygen cavities of the interlayer surfaces. Therefore, no significant intercalation chemistry based on cation exchange reactions is observed for both groups. On the other hand, in the smectite and vermiculite groups of clays with intermediate layer charge densities, diverse intercalation chemistry has been established due to their the appreciable swelling and cation exchange properties.⁶

I-2. Pillared Clays as Two-dimensional Microporous Material

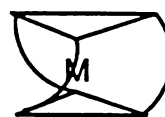
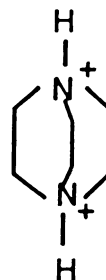
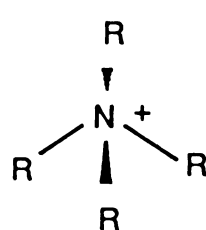
Two different types of intercalated clays are distinguished from the point of view of gallery(interlayer region) environments. One group is the simple hydrated metal cation exchange forms (Mⁿ⁺, n=1,2), such as the smectite group clay minerals, typically found in nature. In these exchange forms, the interlayers collapse at high temperature (above 200 °C) due to the loss of water. This kind of system requires a swelling agent to provide access of other species to the interlayer region. The second type of intercalated clay is the pillared clays in which robust cations act as

props to prevent interlayer collapse even in the absence of a swelling agent. Pillaring means here the creations of accessible micropores in the interlayer regions of the clay by chemical and physical processes based on the cation exchange property of the 2:1 type clays. Pillaring is shown schematically in Fig. 3(a).⁷

The first pillaring of 2:1 type clays was demonstrated by Barrer and MacLeod⁸ by utilizing tetraalkylammonium ions as pillaring species and a smectite clay as the layered host. Several variations in both the pillaring species and layer types have been tried.⁹ Among the typical pillaring agents illustrated in Fig. 3(b), organic-containing molecular pillaring species, such as alkylammonium cations and metal chelate compounds, have been used greatly because of big advantages in defining the shapes and sizes of pillars in the clay galleries.¹⁰ There has been increasing interest in the catalytic properties of pillared clays.¹¹ Various types of inorganic pillaring species have been examined in order to achieve higher thermal stability and larger pore sizes. Al,¹² Zr,¹³ Fe,¹⁴ Cr,¹⁵ and Ti polynuclear hydroxy-oxo cation¹⁶ intercalation reactions afford more thermally stable and catalytically active pillared clays. Usually, pillared clays derived from inorganic cationic species are stable above 500 °C and exhibit large surface areas (BET: 200-500 m²/g) and large pore volumes (0.1-0.2 cm³/g) with relatively large pore diameters (8-20 Å). The distributions of metal oxide



(a)



(b)

Fig. 3 (a) Schematic representation of the pillaring of clay. \oplus and P^+ are simple and robust cations, respectively.
 (b) Typical types of pillaring agents: tetraalkylammonium; bicyclic amine cations; polyhydroxyl or oxo cations; metal chelates.

pillars and pores in the interlayer regions of metal hydroxy cation pillared clays can be highly regular,¹⁰ even though the layer charge densities of smectites vary as much as a factor of 2 from layer to layer.¹⁷

The pores created by pillaring reactions provide chemists with a constrained reaction environment and a system of interconnecting pores for conducting chemical conversions. Chemical reactions within pores may be different from those on bulk surfaces due to differences in kinetic and shape-selective effects.¹⁸ For pores of less than 40 Å diameter, theoretical calculations based on kinetic theories¹⁹ show that great reactivity increases, as much as four orders of magnitude, as well as selectivity increases of 1 or 2 orders of magnitude, can be realized for non-diffusion controlled chemical reactions when the walls of the pores are involved as catalytically active sites. High temperature reactions, such as oil cracking on zeolites or acidic pillared clays can be good systems for testing these small pore effect predictions.

Another important point regarding pillared clays is the high possibility of forming large pores (above 20 Å in diameter) formation which may be very useful for the diffusion of large molecular species into active surface sites.¹⁰ It is well-known that the pore size of pillared clays can be increased simply by increasing the size and charge of the pillars or by the decreasing the charge density of the clay layers.¹⁰

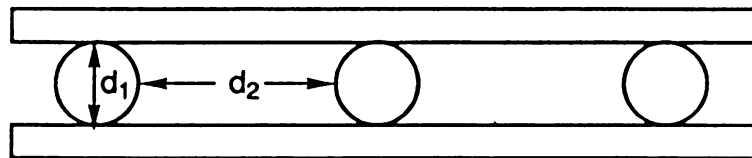
I-3. Transverse Layer Rigidity and Access in Pillared Clays

With regard to the two-dimensional molecular sieving and catalytic applications of pillared clays, one of the very important factors to be considered is the interlayer access phenomena of the species to be catalyzed or to be absorbed. The interlayer access in the pillared clay system is controlled by the size of pores and the size and shape of the species to be accessed.

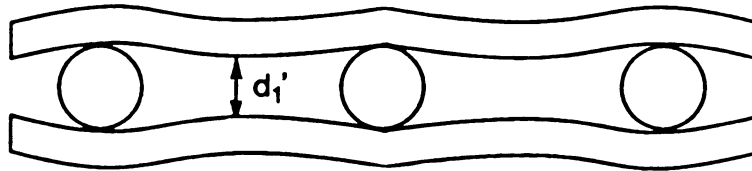
As depicted in Fig. 4(a), the pore size of a pillared clay may be defined by two factors: d_1 , the pillar height and d_2 , the lateral separations between pillars. However, this description is accurate only if the layers are rigid against transverse distortions, such as sagging due to the interlayer interactions or other external forces.

In the case of flexible layers, which are schematically shown in Fig. 4(b), the pore size is not defined well by the above two parameters. Thus, the shortest vertical distance between layers d_1' is expected to be smaller than d_1 .

In spite of the successful pillaring of 2:1 type clays, which proves that the layers are reasonably rigid, transverse distortions of 2:1 clay layers in the range of 10^2 Å have been directly observed by using electron microscopy. Bending of vermiculite layers and folding of smectite layers have been reported.²⁰ Definitely, the 2:1 clay layers have finite rigidity.²¹



(a)



(b)

Fig. 4 Schematic representation of the layers
of a pillared clay assuming
(a) Rigid layers
(b) Flexible layers

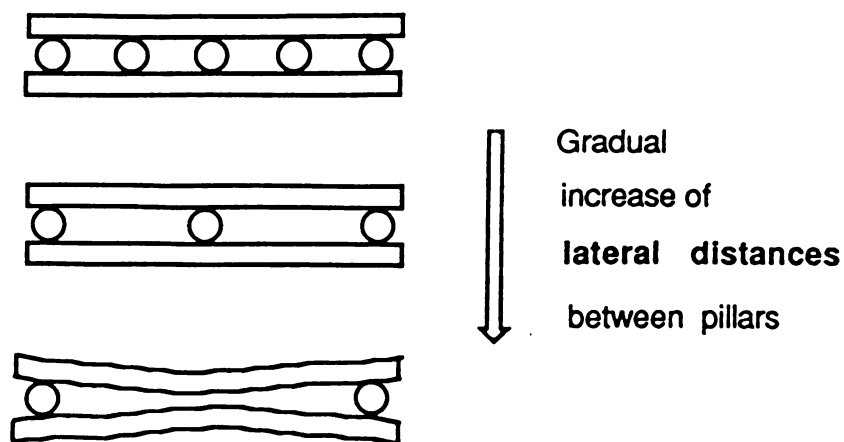
Therefore, it is very important to describe the rigidity of the 2:1 clay layers in order to obtain a better understanding of access phenomena in pillared clays.

This layer rigidity argument is also relevant to the design of large pores in pillared clays. In principle, by increasing the lateral distances and pillar height, the pore size may be increased. However, it is expected that gallery collapse due to interlayer interactions also will increase with increasing lateral separation of the pillars. Thus, the extent of gallery collapse will depend on the transverse layer rigidity of the host layer. Here, the term "transverse layer rigidity" refers to the tendency of a layer to resist transverse (out-of-plane) distortions.

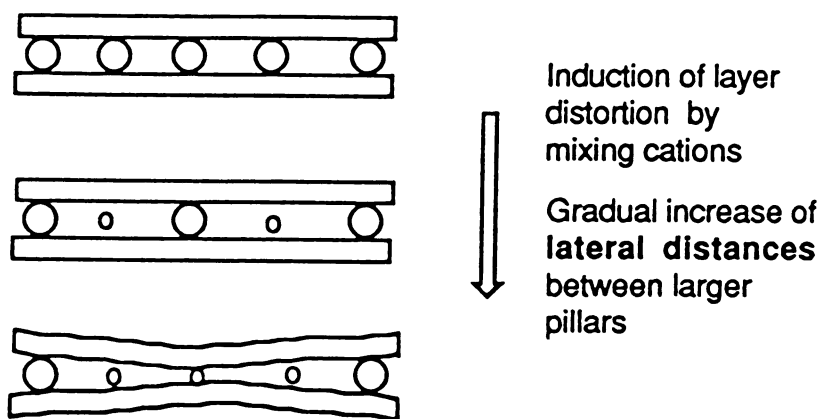
In designing a large-pore pillared clay system, one should be aware of the importance of the transverse layer rigidity of the host layers.

I-4. Approach to Characterizing the Transverse Rigidity of Clay Layers

As described previously, the extent of layer distortion in a pillared clay should be a function of the lateral separation between pillars. Therefore, measuring the average basal spacing as a function of pillar density, as shown in Fig. 5(a), would be an ideal way of probing layer rigidity. However, varying the pillar density would require varying



(a)



(b)

Fig. 5 (a) The concept of probing layer distortions by increasing lateral pillar separation.
(b) The concept of probing layer distortions by mixing large and small ions in a mixed ion clay

either the layer charge on the clay or the charge on the pillars. Neither of these approaches, however, are plausible over suitably broad ranges of pillar densities.

Another more promising route to probing layer rigidity is to induce layer distortions by mixing two cations of different size in the same clay gallery. The term "mixed ion clay" refers to a clay system in which two cations of different kinds are randomly distributed in the same interlayer region.²² The mixed ion clay system is represented by the general formula of $[A]_x[B]_{1-x}-Y$, where "A" and "B" are interlayer cations and "Y" indicates the host clay system. In the above formula, the size of the "A" cation is larger than that of the "B" cation by definition. In a mixed ion clay, the lateral distances between larger cations can be changed almost continuously from the limiting value of homoionic $[A]-Y$, to infinity by changing the ratios of two different cations. (see Fig. 5(b))

Since the magnitude of the layer distortion should be small compared to the size of the layer, one dimensional X-ray diffraction from stacked clay layer samples could be used to detect layer distortions which change in the repeat distance of the layers along the c axis.²³

Fig.6 illustrates the expected behavior for two extreme cases of mixed cation pillared clays: the infinitely rigid limit (Fig. 6a) and the infinitely floppy limit (Fig. 6b). The expected normalized basal spacings (d_n), relative responds of repeating distances in mixed ion clays, defined

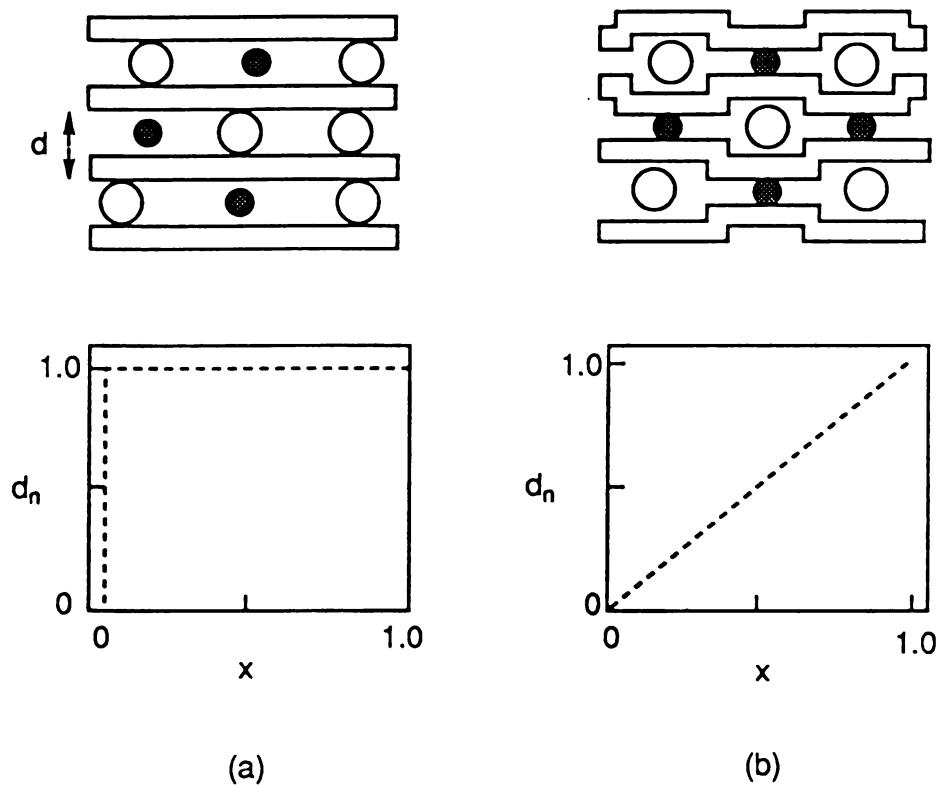


Fig. 6 Schematic representation of the expected relationship between d_n and x in $[A]_x[B]_{1-x}-Y$.
 (a) Infinitely rigid layers
 (b) Infinitely flexible layers

as $d_n(x) = (d(x) - d(0)) / (d(1) - d(0))$ where $d(x)$ is the d-spacing of the mixed ion clay at a concentration x of the larger cation, are also plotted in the lower part of the figure. For the infinitely rigid layer case (a), d_n reaches 1 at a very low concentration of the "A" cation, ideally, corresponding to only three "A" cations per gallery. For the infinitely floppy limit, the situation is totally different. In this case, the layers fluctuate locally in accord with the cation size and this results in a linear relationship between $d_n(x)$ and x .

Since the real 2:1-type clays with finite layer rigidities do not belong to either of the two extreme cases, it is expected that the shape of the $d_n(x)$ vs. x plot will be intermediate between these of two extreme cases.

Based on the above considerations of the behavior of $d_n(x)$ vs. x , it may be concluded that layer rigidity information can be extracted from $d_n(x)$ vs. x plot, provided that an appropriate model can be developed.

In order to experimentally quantify the transverse distortions of 2:1 clay layers, one must achieve the following goals: (i) the synthesis and characterization of a series of mixed-ion clays, (ii) determination of the $d_n(x)$ vs. x plot for the mixed-ion clay system, and (iii) establish a suitable model for the simulation of the $d_n(x)$ vs. x dependence and extract a layer rigidity parameter from the experimental results.

I-5. Defining the Mixed-Ion Clay System

Llano vermiculite, which has layer charge density as high as the natural micas,²⁴ served as the clay host for this research. The high charge density is preferred for the simulation experiments, because the symmetry and locations of the intercalated cations can be reasonably deduced. As indicated in the early part of the introduction, the location and symmetry of cations in micas are well-defined. It can be assumed that the distribution of cations in Llano vermiculite is almost the same as that of micas.

Trimethylammonium and tetramethylammonium cations were utilized in synthesizing the mixed cation clays, because of the suitable swelling properties of trimethylammonium and tetramethylammonium exchange forms of Llano vermiculite.

II. EXPERIMENTAL

II-1. Materials

Tetramethylammonium chloride and trimethylamine were purchased from Aldrich Chemical Co. and used without further purification. Single crystals of Llano vermiculite were obtained from the Source Clay Repository at the University of Missouri, Rolla, Missouri. The crystals were ground in a mortar and pestle to a fine powder (-200 mesh). Then, the powdered form of the vermiculite was treated with 2.0 M MgCl_2 solution for one day at room temperature to ensure complete saturation of the exchange sites by Mg^{2+} . After the separation of the clay from suspension by repeated centrifugations and decantations, the Mg-vermiculite was dried in air for at least two days. The quality of vermiculite was sufficient to prepare all of the mixed ion derivatives used in this study.

II-2. Synthesis

II-2-1. $[(\text{CH}_3)_3\text{NH}^+]$ -Vermiculite

The trimethylammonium exchange form of vermiculite was obtained by ion exchange of the pristine mineral in the presence of EDTA anion as a complexant for magnesium ion. A solution containing 12.5 wt% trimethylamine and 2.7 wt% ethylenediaminetetraacetic acid was adjusted to pH=7.0 by the slow addition of concentrated HCl. This solution was mixed with powdered magnesium vermiculite in the ratio 1.0 g of clay per 200 ml of exchange solution, corresponding to a Mg^{2+} : $(\text{CH}_3)_3\text{NH}^+$: EDTA molar ratio of 1:560:50. The reaction mixture was allowed to stir vigorously for one day at room temperature. The $[(\text{CH}_3)_3\text{NH}^+]\text{-V}$ (V: vermiculite) was recovered by five cycles of centrifugation and washing with 200 ml quantities of distilled water. The x-ray diffraction pattern of an oriented film sample dried at 100°C exhibited a basal spacing of 12.70 Å.

II-2-2. $[(\text{CH}_3)_4\text{N}^+]\text{-Vermiculite}$

This derivative was prepared from $[(\text{CH}_3)_3\text{NH}^+]\text{-V}$ by ion exchange reaction with the $(\text{CH}_3)_4\text{N}^+$ cation. To a 2.5 M solution of $(\text{CH}_3)_4\text{NCl}$, an equal volume of 1.0 wt% of $[(\text{CH}_3)_3\text{NH}^+]\text{-V}$ suspension was added at room temperature. After 24 hours of stirring at room temperature, the $[(\text{CH}_3)_4\text{N}^+]\text{-V}$ was washed by successive centrifugation (15,000 rev/min), decantation and redispersion into distilled water. Analysis for trimethylammonium ion (see below) indicated

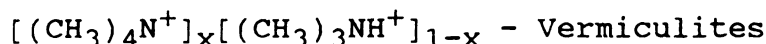
that the exchange reaction was 96% complete. An oriented film sample dried at 100 °C exhibited an x-ray basal spacing of 13.34 Å.

II-2-3. Mixed Ion $[(CH_3)_4N^+]_x[(CH_3)_3NH^+]_{1-x}$ Vermiculites

Mixed ion exchange forms of $[(CH_3)_4N^+]_x[(CH_3)_3NH^+]_{1-x}-V$ were prepared by the reaction of $[(CH_3)_3NH^+]-V$ suspensions with $(CH_3)_4NCl$ solutions at various $(CH_3)_4N^+$ molar ratios. The concentration of the $(CH_3)_4N^+$ was in the range of 0.0024-2.500 M. After allowing the reaction mixtures to be stirred for designated reaction times at room temperature, the mixed-ion vermiculites were collected by using the same isolation procedures as described previously.

II-3. Characterization

II-3-1. Exchange Ion Compositions of



The exchange ion compositions of $[(CH_3)_4N^+]_x[(CH_3)_3NH^+]_{1-x}$ -vermiculites were determined from the amount of trimethylamine released upon dispersing a fixed amount of the mixed-ion clay in 1:1 methanol water(volume ratio) mixture containing 0.05 M NaOH. The liberated trimethylamine was slowly transferred by distillation into a

titration flask equipped with a pH electrode and a buret containing standard HCl solution. During the distillation process, the pH of the solution in the titration flask was kept just below a value of 7 by the periodic addition of a standard HCl solution. The amounts of HCl consumed for the mixed ion clays were compared directly with the amount needed to neutralize the trimethylamine liberated from an equivalent quantity of $[(CH_3)_3NH^+]$ -vermiculite.

II-3-2. X-ray Diffraction Patterns

Oriented film samples for X-ray diffraction analysis were prepared by drying approximately 1 ml of a 1 wt% clay suspension on glass slides in air. The films were then dried in an oven at 100 °C. The mosaic spreads of the small clay platelets in the films were 5-10 degrees.²⁵ No swelling by water was observed upon exposure of the heated samples to the atmosphere for prolonged periods of several months. Diffraction patterns were obtained using Ni-filtered Cu-K α radiation. The basal spacings were determined from the slopes of Q vs. l plots where Q is the momentum transfer, $(4\pi \sin \theta / \lambda = 2\pi l / d)$ and l is the diffraction order. The slopes of the Q vs. l plots were determined by weighted linear-least square regression analysis.²⁶

II-3-3. Modeling X-ray Diffraction Patterns

In order to interpret the xrd patterns of samples in terms of gallery ion distributions, one-dimensional xrd patterns were generated based on the three known models: Bragg, Hendricks-Teller,²⁷ and Reynolds models.²⁸

In the Bragg model, the homogeneous mixing of two different kinds of cations in the same gallery is assumed. However, in the two other models, the segregation of two different kinds of cations into different galleries is assumed and modeled by appropriate mathematical treatments.

Details of the treatment of the xrd pattern calculations are summarized in Appendix I. Layer atomic coordinates were taken from the single crystal structure determination of vermiculite.²⁹ The X-ray scattering factors of the clay layer atoms were taken from the values provided by Wright.³⁰

II-3-4. MacEwan Direct Fourier Transform of XRD Patterns

In order to determine the sequences of layer stacking, diffraction patterns were transformed into the function $W(R)$ ²⁸, which is the probability of finding a given layer to layer distance R . In this equation (see Eq. 1), I_s is the diffraction intensity at angle θ , LP the Lorentz-polarization factor, $|G|^2$ the squared magnitude of the layer factor, Q the momentum transfer, and R a distance in unit

of Å. This transform is a modification of the Patterson function³¹, which is used to obtain the vectorial separation of atoms within an unit cell. In the calculation, the sum was taken over the continuous diffraction profile and the structure factor of trimethylammonium vermiculite was used.

$$W(R) = \sum_{\theta} \frac{I_s}{LP |G|^2} \cos(RQ) \quad (1)$$

II-3-5. Infrared Spectroscopy

Infrared spectroscopy was used mainly to obtain information on the orientation of the smaller trimethylammonium ions in the galleries. The absorptions of the N⁺-H stretching frequency at about 2730 CM⁻¹ were compared with changes in "the angle of incidence" between the surface of the self-supported clay film and the incident infrared beam.

An IBM FT-IR spectrometer model 40S was used to obtain the spectra.



II-3-6. Raman Spectroscopy

Laser Raman spectroscopy was used to examine the mixed-ion clays. The in-plane intralayer torsional mode of tetrahedral alumino-silicate sheets³² was examined to determine the effect of the cation mixing on this vibrational mode.

Raman spectra were obtained using the 5145 Å line of an argon laser at a typical power level of 150 mW. All measurements were made with the scattered light collected at 90 degrees to the direction of propagation of the laser light, which was incident at an angle of about 45 degrees to the sample plane. The experiments were undertaken at room temperature.

II-3-7. Chemical Analysis

Chemical analysis on independent samples of Llano vermiculite were accomplished using ICP atomic emission spectroscopy. The NBS 98-a plastic clay served as a standard clay for the analysis.

With regard to the preparation of the sample solutions, about 30 mg of Mg-vermiculite was mixed with 0.3 g of LiBO_2 in a graphite crucible, and the mixture was fused in a furnace at 1000 °C for 10 minutes. The molten material was poured into 30 ml of 10 % HNO_3 and the solution was stirred

to achieve complete dissolution. The elements Mg, Al, and Si were analyzed.

II-4. Modeling the Composition Dependence of Gallery

Height for $[(\text{CH}_3)_4\text{N}^+]_x[(\text{CH}_3)_3\text{NH}^+]_{1-x}$ - Vermiculite

To help us understand the behavior of $d_n(x)$ on x in mixed ion $[\text{A}]_x[\text{B}]_{1-x}$ -clays, we generated, in collaboration with Professor Mahanti and Solin and their students, $d_n(x)$ vs. x data for mixed ion $[\text{A}]_x[\text{B}]_{1-x}$ -vermiculite model systems containing monolayers of pillaring ions between clay layers with finite transverse rigidity. For simplicity, we assumed that the pillaring ions are rigid spheres positioned at the centers of the hexagonal cavities defined by the Kagome lattice of the gallery surfaces. These pillar positions define a two-dimensional triangular lattice of lattice constant $a_0 = 5.34 \text{ \AA}$.

Starting with a single gallery in which each pillar position is occupied by a smaller "B" ion of height d_B , we randomly replaced the "B" ions with larger "A" ions of height d_A . The height of the gallery within a healing length is assumed to increase from d_B to d_A upon replacement of "B" by "A". Here, the healing length is a distance from the layer position of a "A" cation which is surrounded by only "B" cations to the layer positions at which the layer returns to $d(0)$. A second "A" ion within the healing length

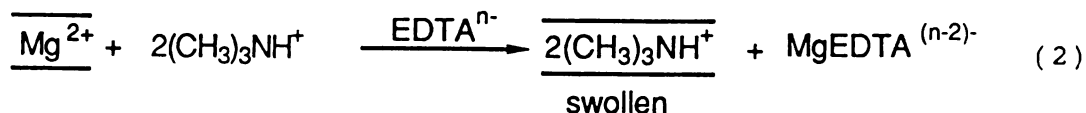
of a first "A" ion does not affect the already expanded unit cells, but it expands unexpanded cells within its healing length . The process of random replacing the "B" ions continues until $x=1$. The $d_n(x)$ values are determined by the fraction of expanded triangular cells.

III. RESULTS

III-1. Synthesis

Naturally occurring single crystals of Mg^{2+} -vermiculite (Llano, Texas) served as the starting mineral for the synthesis of our mixed alkylammonium ion clays. The results of independent chemical analysis for Mg, Al, and Si indicated the unit cell formula to be: $\text{Mg}_{0.86}^{2+}(\text{Si}_{5.87}\text{Al}_{2.13})[\text{Al}_{0.48}\text{Mg}_{5.52}]\text{O}_{20}(\text{OH})_4$. In order to enhance the ion exchange reactivity of the parent Mg-vermiculite, the particle size was reduced by wet grinding in water to -200 mesh sizes.

The reaction of the powdered Mg^{2+} -vermiculite with excess $(\text{CH}_3)_3\text{NH}^+$ and EDTA anion as a complexant of Mg^{2+} afforded $[(\text{CH}_3)_3\text{NH}^+]$ -vermiculite in quantitative yield as expressed in Equation 2, wherein the horizontal lines represent the clay layers.



The presence of the EDTA anion was essential for complete exchange. In the absence of the complexant,



complete exchange could not be achieved even after six reaction cycles of the Mg^{2+} -vermiculite with $(\text{CH}_3)_3\text{NH}^+$ solutions under the forcing reaction condition defined in Fig. 7.

The complete replacement of hydrated magnesium ions by the trimethylammonium cations in the presence of the EDTA anion results in the swelling of the interlayer region by water. The degree of swelling was very extensive, as evidenced by gel formation at concentrations of 10 wt% clay and 90 wt% of water. The swelling phenomenon and associated layer exfoliation most likely leads to the further reduction of the clay platelet size. Thus, the final $[(\text{CH}_3)_3\text{NH}^+]$ -vermiculite product is no longer in the form of single crystal particles. Instead, the clay layers are aggregated as turbostratic tactoids with regular stacking in the direction perpendicular to the layer but random in-plane orientations. Analogous layer aggregation mechanisms have been found for smectite clays with 2:1 layer lattice structures.³³

The reaction of Mg^{2+} -vermiculite with tetramethylammonium ion in aqueous solution under conditions analogous to those used to prepare the trimethylammonium derivative ($\text{Mg}^{2+}:\text{Me}_4\text{N}^+:\text{EDTA}=1:560:50$) yielded only partial replacement of the interlayer magnesium ions by tetramethylammonium ions because of the precipitation of the EDTA anion by tetramethylammonium cation. The exchange reaction with tetramethylammonium in the absence of EDTA anion also showed

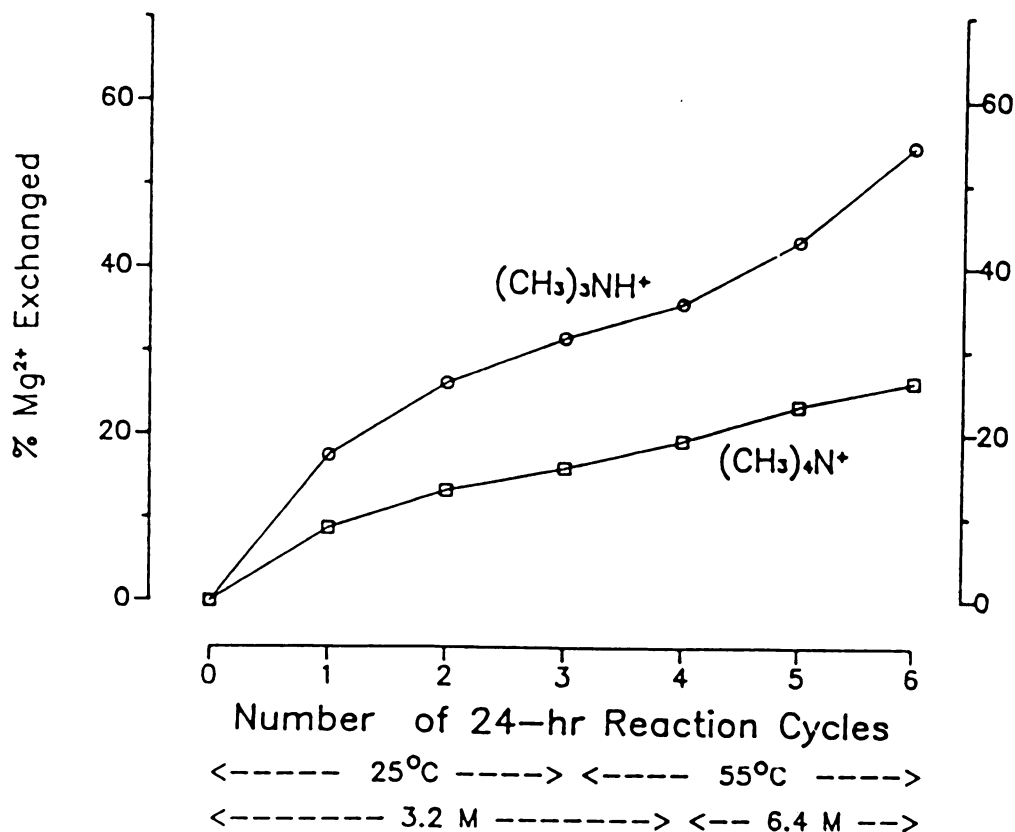
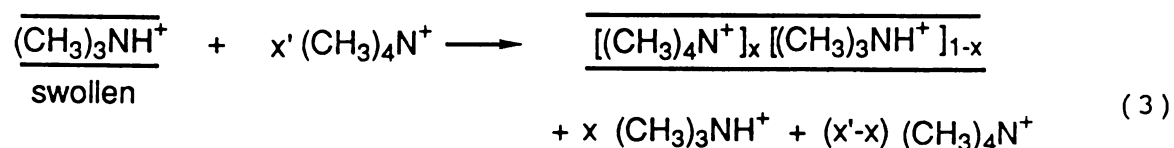


Fig. 7 Plots for comparing of ion exchange reactivity of powdered Mg^{2+} -vermiculite with $(\text{CH}_3)_3\text{NH}^+$, and $(\text{CH}_3)_4\text{N}^+$ in the absence of EDTA anion. After each 24 hour reaction period, the ion exchange solution was replenished with a fresh solution containing an excess of alkylammonium ion. The ratio of alkylammonium ion : Mg^{2+} was 54:1 for the first four reaction periods, and 108:1 for the last two reaction periods.

a very slow exchange rate compared to that of the trimethylammonium case, as shown in Fig. 7. The slow migration of tetramethylammonium ions may be due to their lack of hydration within the clay galleries.

The differences in the solvation properties of the trimethylammonium and tetramethylammonium cations in the galleries of the host clay provided the key to the synthesis of the mixed ion derivatives. The addition of controlled amounts of tetramethylammonium ion to $[(\text{CH}_3)_3\text{NH}^+]$ -vermiculite suspensions resulted in the flocculation of the suspension and the concomitant replacement of some $(\text{CH}_3)_3\text{NH}^+$ ions by the desired $(\text{CH}_3)_4\text{N}^+$ ions of larger size. Because flocculation is rapid, the segregation of the exchange ions into separate galleries is impeded. Consequently, the distribution of the two ions within the galleries is under kinetic control rather than thermodynamic control. Equation 3 summarizes the overall reaction for mixed ion synthesis.



The chemical compositions of the mixed ion products were determined by displacing the alkylammonium ions with sodium cation as shown in Equation 4, and subsequent titration of the liberated trimethylamine with standard HCl solution.

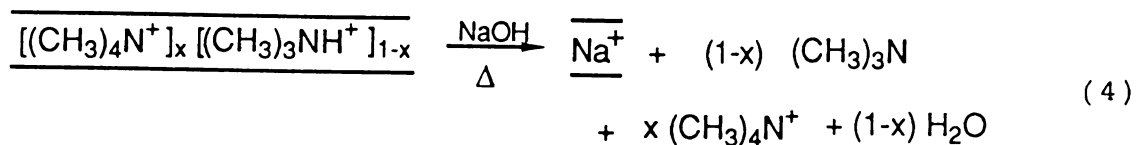


Table 2 provides the compositions of some representative mixed-ion products obtained by the reactions of $[(CH_3)_3NH^+]$ -vermiculite with $(CH_3)_4NCl$ according to Equation 3. It is noteworthy that the $(CH_3)_3NH^+$ ions are easily displaced by the $(CH_3)_4N^+$ ions at low values of x . In order to achieve mixed ion products with high values of x , however, a large excess of tetramethylammonium ion was necessary.

III-2. X-ray Diffraction

Fig. 8 illustrates the diffraction patterns for $(CH_3)_3N^+$ -vermiculite as a freshly prepared wet gel, an air-dried oriented film, and an oriented film dried at 100 °C. The gel form of the sample is essentially X-ray amorphous. Only very weak reflections by a small non-clay impurity phase were detected. This means there is no long range order of layers within the x-ray correlation distances in the sample. The air-dried sample exhibits two broad 001 reflections indicative of an interstratified system containing at least two basal spacings due to different

Table 2. Compositions of Representative $[\text{Me}_4\text{N}^+]_x[\text{Me}_3\text{NH}^+]_{1-x}$ -Vermiculites
Obtained by Reaction of $[\text{Me}_3\text{NH}^+]$ -Vermiculite with Aqueous Me_4NCl

Vol. of 1 wt% Me_3NH^+ - Vermiculite, mL	Vol. of $[\text{Me}_4\text{N}]\text{Cl}$, mL	Initial Conc. $[\text{Me}_4\text{N}]\text{Cl}$, M	Fraction of Total Onium Ions as $[\text{Me}_4\text{N}]^+$	Value of x in Mixed Ion Product
20.0	20.0	0.0024	0.13	0.14
20.0	20.0	0.014	0.47	0.41
20.0	20.0	0.080	0.84	0.63
20.0	20.0	0.73	0.97	0.86
20.0	20.0	2.50	0.99	0.96

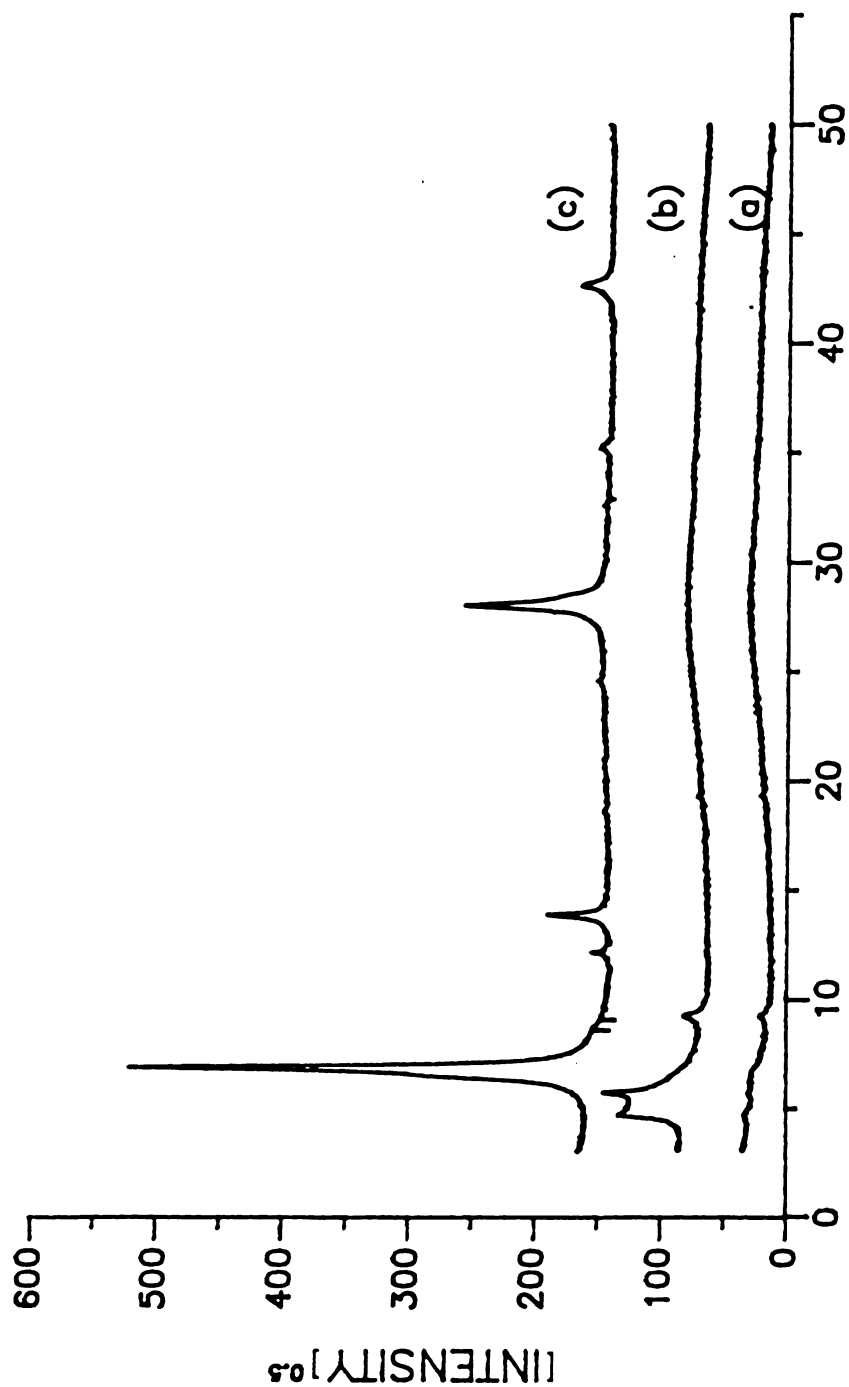


Fig. 8 X-ray diffraction patterns for $(\text{CH}_3)_3\text{NH}^+$ -vermiculite as (a) freshly prepared wet gel, (b) a film dried 1 hr. in air, and (c) an oriented film dried 1 hr at 100°C . All diffraction patterns were recorded under equivalent conditions of x-ray exposure.

water content in the interlayer regions. In addition, the diffraction peak intensities are relatively weak and layer stacking is considered to be incomplete. Upon heating to 100 °C, the pattern sharpens dramatically and multiple orders of reflection are observed corresponding to a single basal spacing of 12.70 Å. Re-exposing the oven-dried sample to air did not result in the re-adsorption of water and no change of d-spacing was detected.

Fig. 9 illustrates the X-ray diffraction patterns for oriented film samples of representatives $[(\text{CH}_3)_4\text{N}^+]_x[(\text{CH}_3)_3\text{NH}^+]_{1-x}$ -vermiculites that have been dried at 100 °C. The presence of multiple orders of 001 reflections with reasonably small band widths indicates a regular distribution of gallery heights for each alkylammonium ion composition.

To obtain further verification of the mixing of two alkylammonium ions within each gallery, we compared the experimental x-ray diffraction patterns with computer-generated patterns according to three models. In order to confirm the structural and compositional inputs for the calculation, the 001 reflections of homo-ionic $(\text{CH}_3)_3\text{NH}^+$ -vermiculite and $(\text{CH}_3)_4\text{N}^+$ -vermiculite were generated (see Appendix I for the details). Fig. 10 and Fig. 11 compare the observed 001 reflections with the calculated Bragg reflections for the homo-ionic $(\text{CH}_3)_3\text{NH}^+$ -vermiculite ($x=0.0$) and $(\text{CH}_3)_4\text{N}^+$ -vermiculite ($x=1.0$), respectively. Reasonable agreements are obtained for the observed and calculated



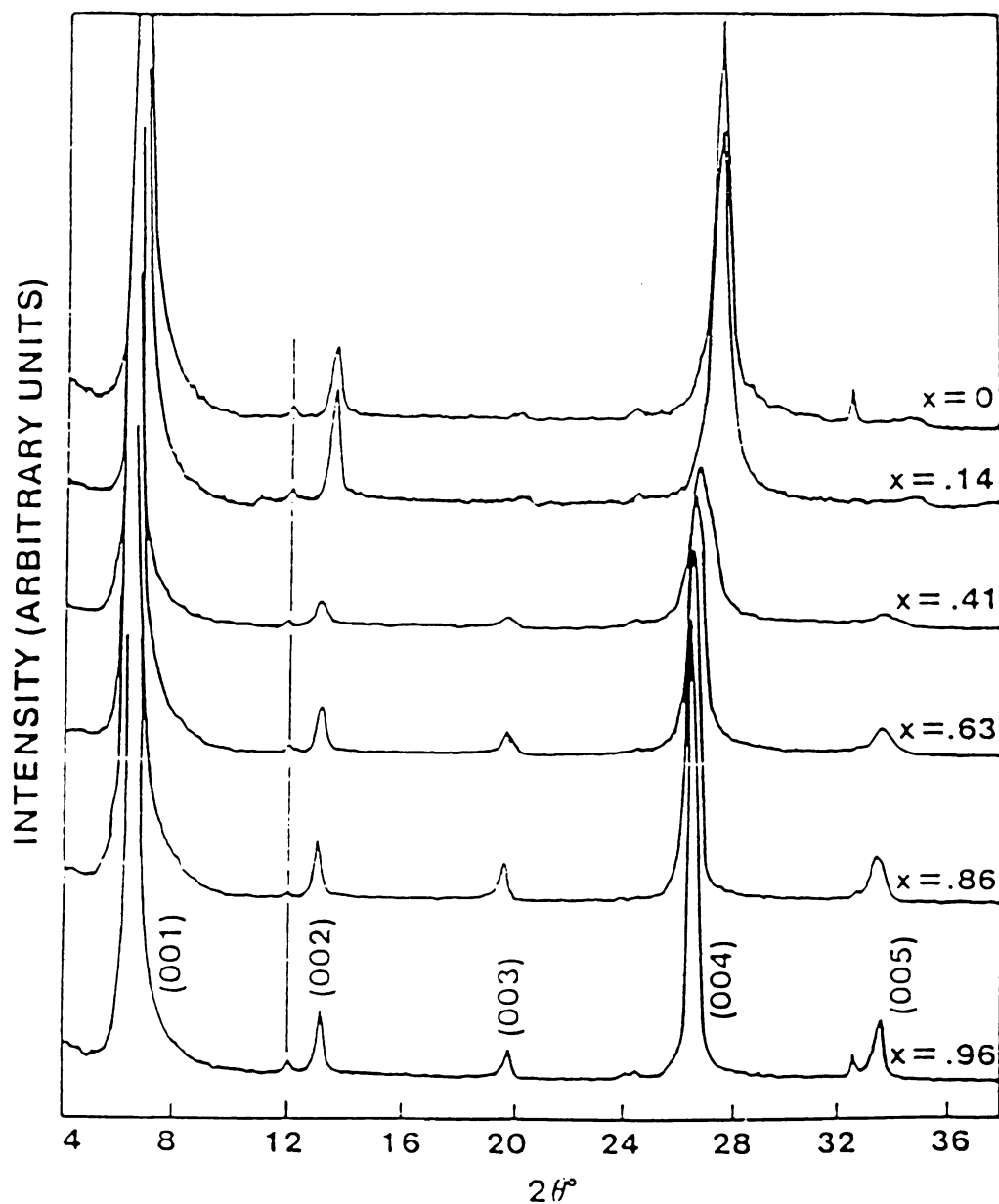


Fig. 9 X-ray diffraction patterns for oriented film samples of representative $[(CH_3)_4N^+]_x[(CH_3)_3NH^+]_{1-x}$ vermiculites heated at 100 °C



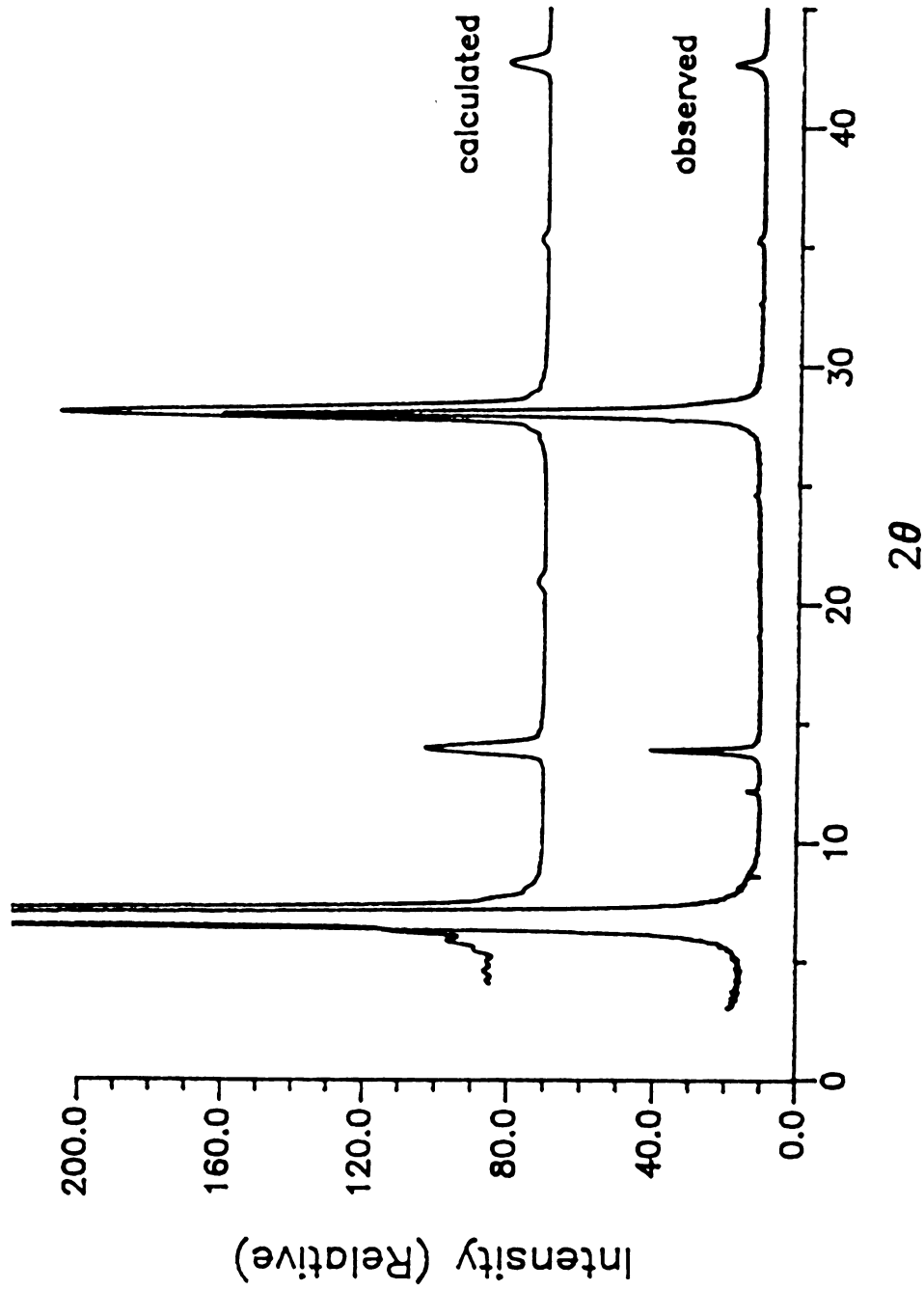


Fig. 10 Comparison of the observed and calculated xrd pattern for homoionic $(\text{CH}_3)_3\text{NH}^+$ -vermiculite

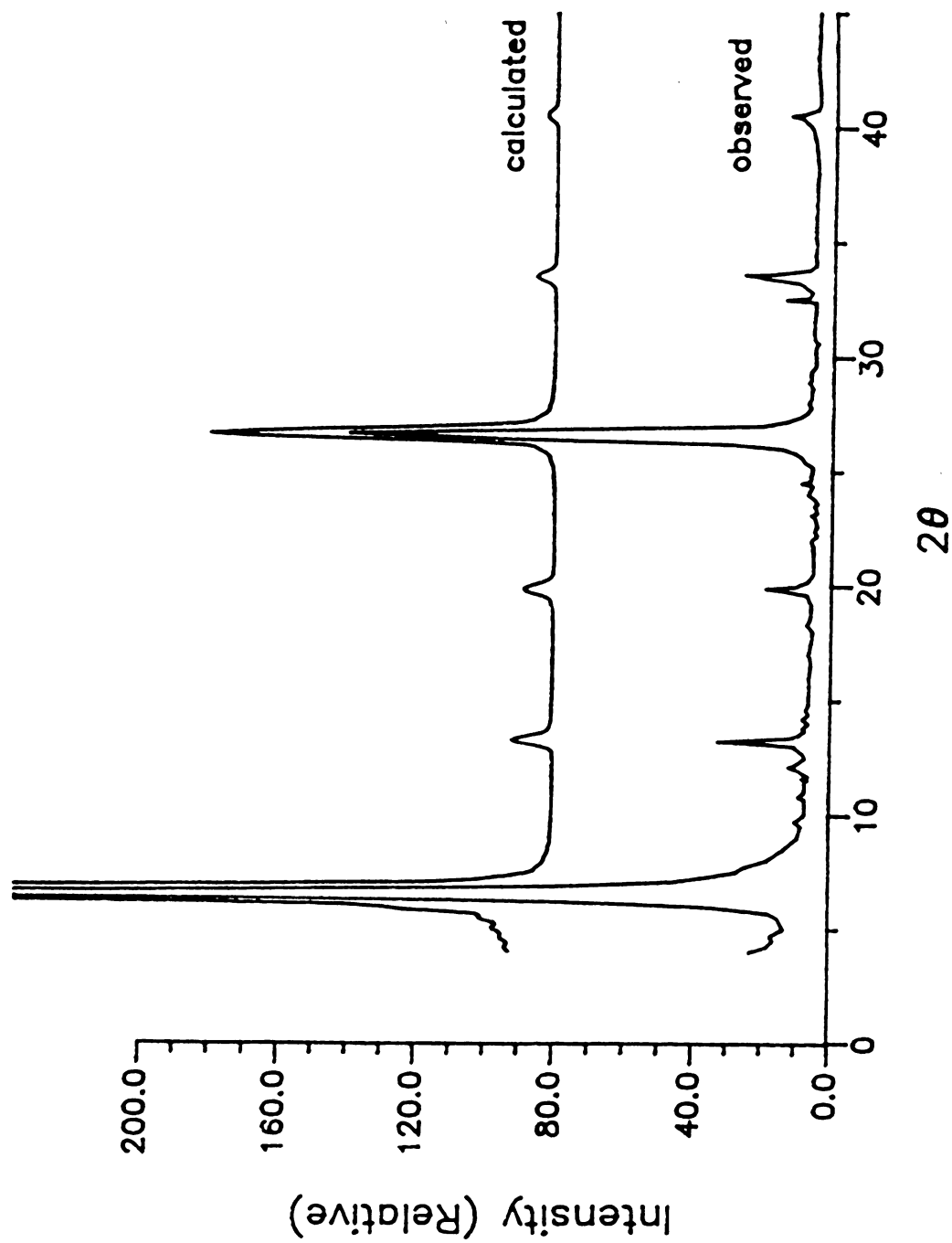
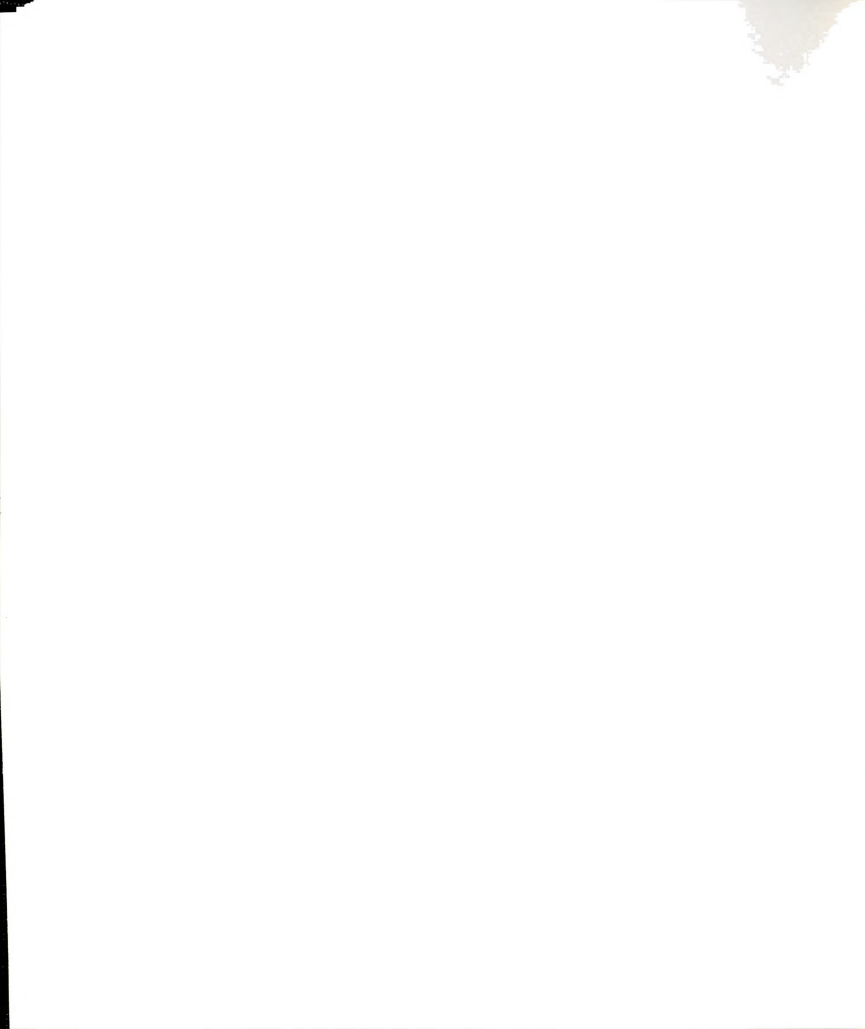


Fig. 11 Comparison of the observed and calculated xrd pattern for homoionic $(\text{CH}_3)_4\text{N}^+$ -vermiculite



relative intensities for homo-ionic derivatives with a single basal spacing. The agreement between the observed and calculated patterns showed that the structure factor assigned to the layer could be used for the calculation of the x-ray diffraction patterns of the mixed-ion $[(\text{CH}_3)_4\text{N}^+]_x[(\text{CH}_3)_3\text{NH}^+]_{1-x}$ -vermiculites.

Fig. 12 illustrates the observed and calculated 001 reflections for $x=0.63$. Clearly, very poor agreements are observed in the positions of the observed and calculated reflections based on Hendricks-Teller and Reynolds models for ion segregation compared to those of the Bragg model for the ion mixing in the galleries. These results strongly suggest that the basic synthetic strategy used in preparing the mixed ion vermiculite samples was successful. (There are some arguments concerning the true gallery x value which should be used in the calculation of 001 intensities. See appendix II.)

We have also performed a MacEwan direct Fourier transform, which is equivalent to a one-dimensional Patterson synthesis based on the whole diffraction profile. This transform provides the lattice vector distribution along the c axis. The probability function $W(R)$ for the mixed ion sample with $x=0.63$ is shown in Fig. 13. Only vector distributions corresponding to a unique $d(x)$ value were observed. Thus, segregation of the two ions into separate phases with $d=13.34$ and 12.70 Å characteristic of the parent homo-ionic intercalates can be precluded. The

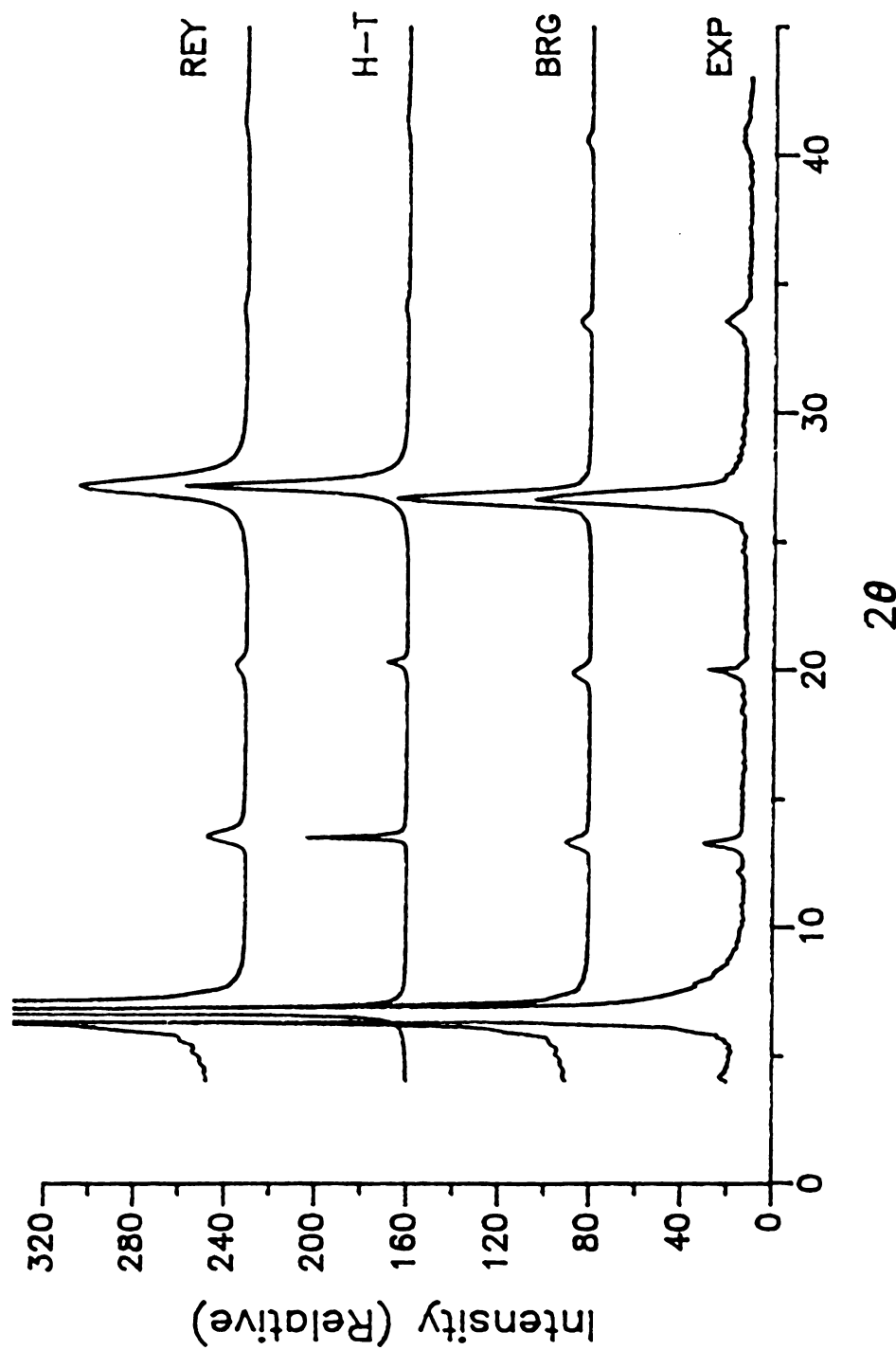


Fig. 12 Comparisons of observed and calculated xrd patterns based on three models for $[(\text{CH}_3)_3\text{NH}^+]_{0.37} - \text{vermiculite}$
 BRG: Bragg model. H-T: Hendricks-Teller model
 REY: Reynolds model, EXP: Experimental pattern

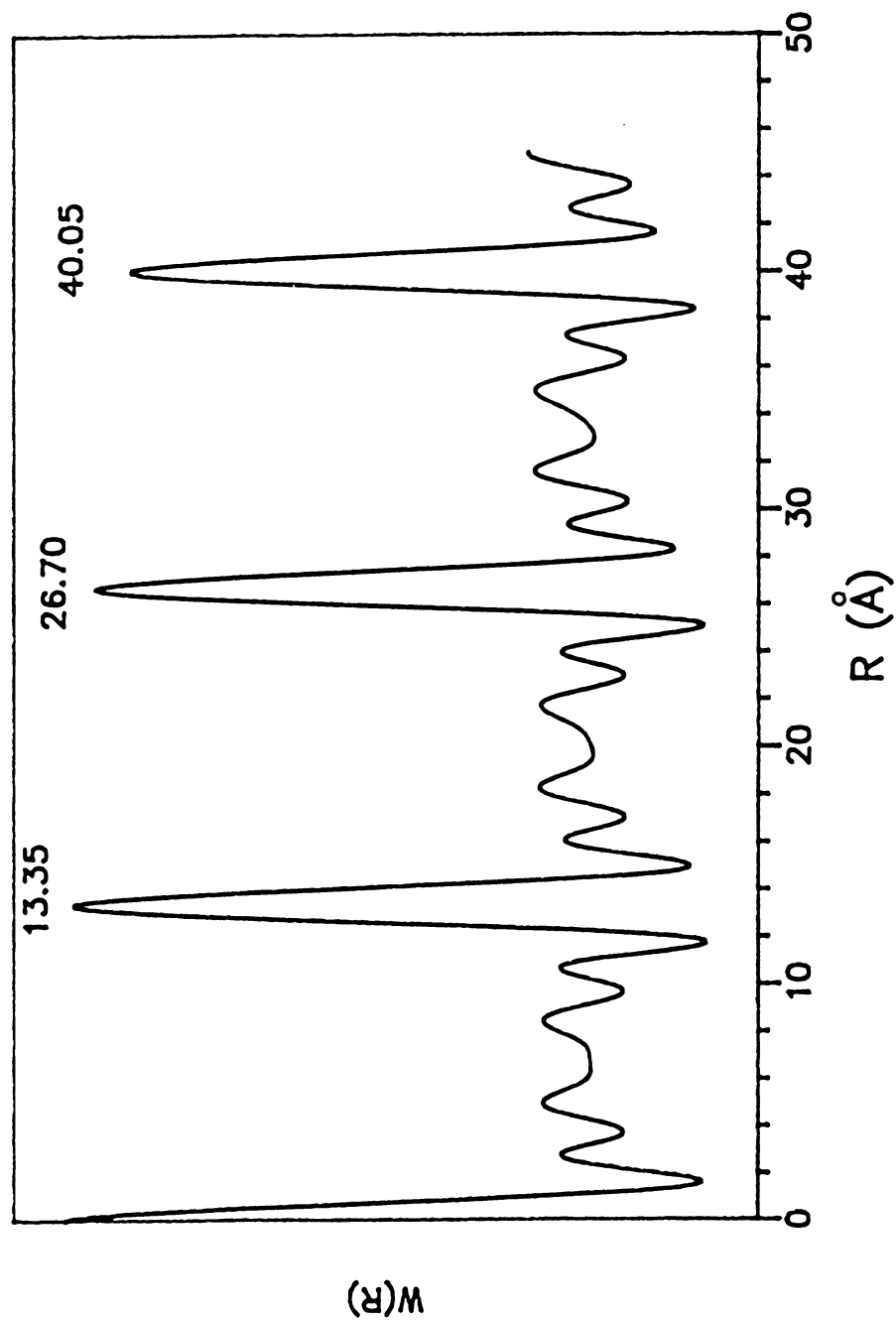


Fig. 13 Direct MacEwan transform of xrd pattern of $[(CH_3)_4N^+]_{0.63} [(CH_3)_3NH^+]_{0.37}$ - vermiculite

absence of peaks at certain R , which corresponds to the sum of these d values, also precludes the possibility of alternating sequences of gallery spacings containing the two ions (ABAB, AAB, BBA, etc.).

Basal spacings for the mixed alkylammonium vermiculites were determined by fitting the observed 001 reflections to the Bragg relationship $Q = 2\pi l/d$ where $Q = 4\pi \sin \theta/\lambda$. Plots of Q versus l are shown for some typical mixed ion vermiculites in Fig. 14. The broken lines in the figure represent the best least square fit in the data points. It is noteworthy that the Q vs l plots exhibit a high degree of linearity, as expected for uniformly mixed systems in which the two ions co-occupy the same galleries. If the two types of alkylammonium ions were demixed with the alkylammonium ions randomly segregated into separate galleries, we would not expect a strictly linear relationship between Q and l .

Fig. 15 illustrates the compositional dependence of the normalized basal spacing, $d_n(x)$ for 27 independent $[(CH_3)_4N^+]_x[(CH_3)_3NH^+]_{1-x}$ -vermiculite samples over the composition range, $x=0$ to 0.96 . Here $d_n(x) = [d(x) - d(0)]/[d(1) - d(0)]$. The basal spacings clearly follow a non-Vegard's law (non-linear) dependence on composition. Particularly noteworthy are (i) the rapid rise in $d_n(x)$ with increasing x near the threshold value of $x_t=0.2$ and (ii) the value of $d_n(x)$ reaches the maximum possible value of 1.0 very near an x value of 0.6.

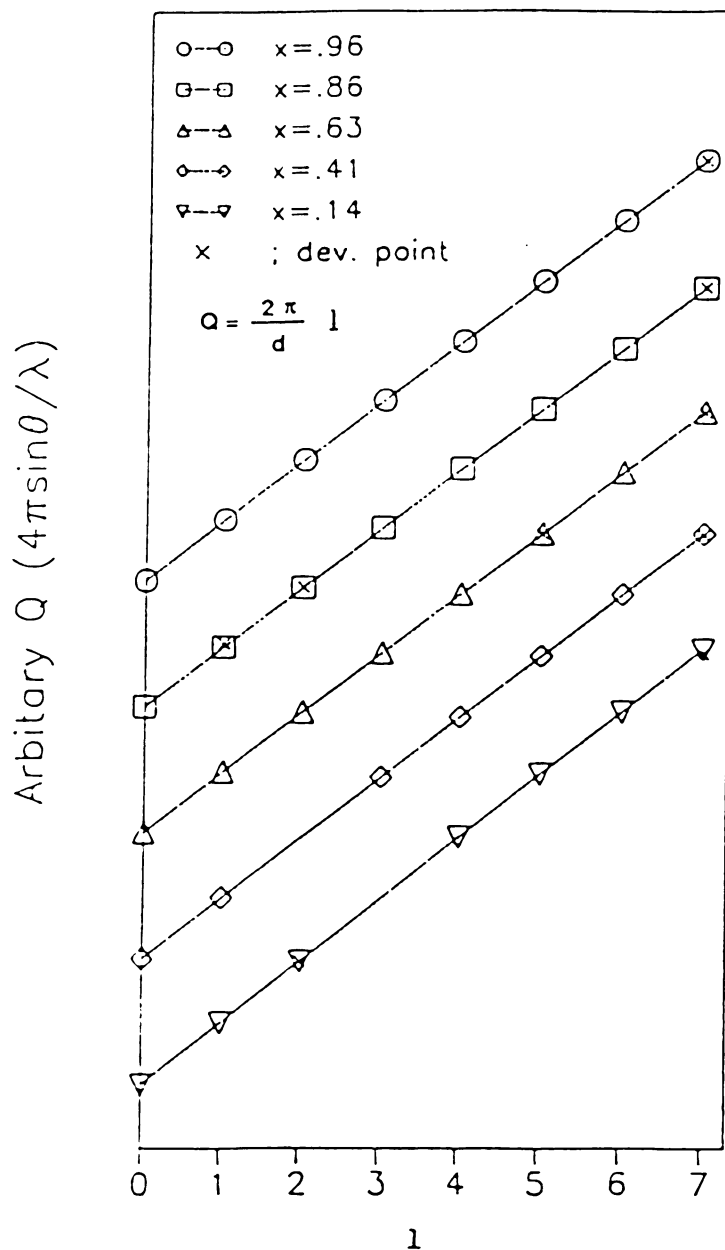


Fig. 14 Representative Q vs l plots for $[(\text{CH}_3)_4\text{N}^+]_x [(\text{CH}_3)_3\text{NH}^+]_{1-x}$ -vermiculites. The broken lines are the best weighted linear least squares fit to the data points.



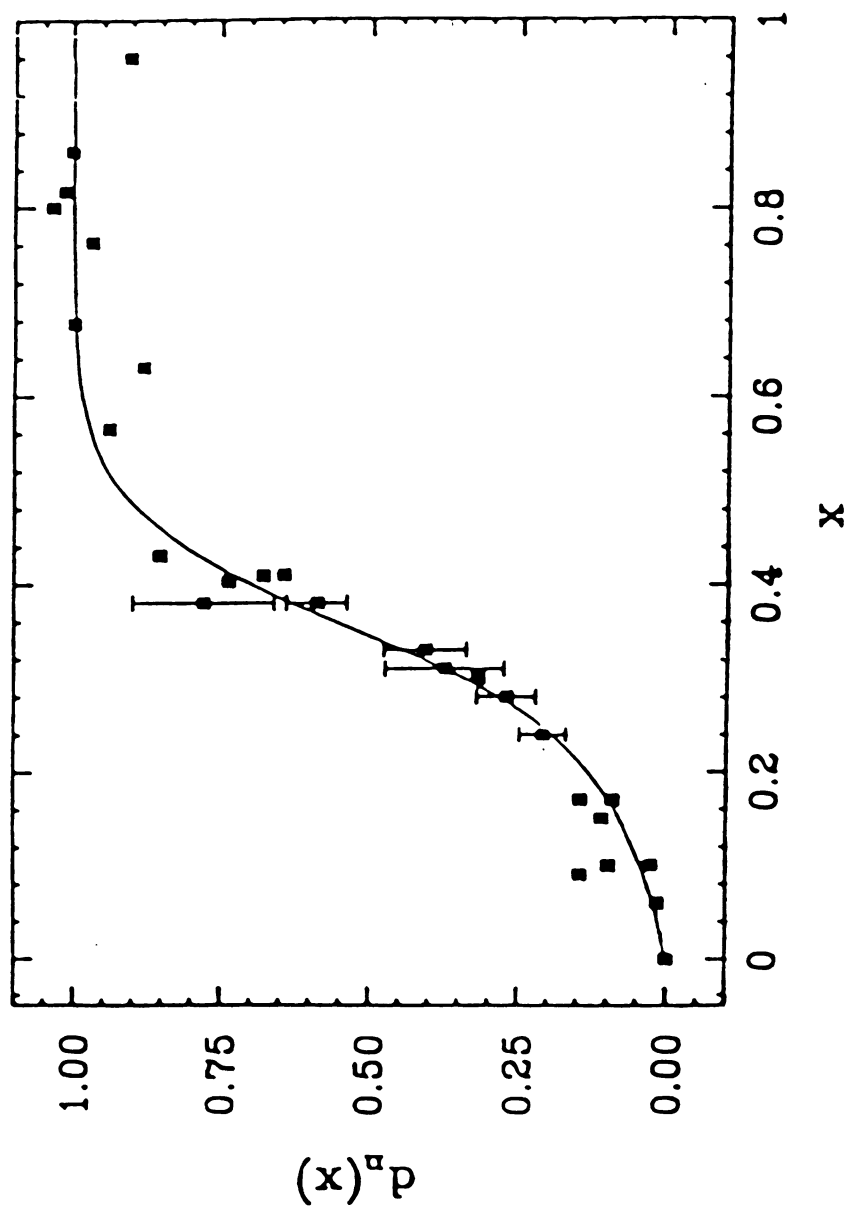


Fig. 15 The composition dependence of the normalized basal spacings for $[(\text{CH}_3)_4\text{N}^+]_x[(\text{CH}_3)_3\text{NH}^+]_{1-x}$ -vermiculites. Solid line is the least square fit to the data using Equation 7 of the text with the following parameter set: $p=8.0$; $f=0.5$; $\Delta/kT=4.3$.

For the comparison purposes, the expected $d_n(x)$ vs. x plot for a ion-segregated $[(CH_3)_4N^+]_x[(CH_3)_3NH^+]_{1-x}-V$ system according to the Reynolds model is shown in Fig. 16. The observed data (Fig. 15) deviate strongly from the expected behavior for an ion-segregated system.

III-3. Generation of $d_n(x)$ vs x Plots for Mixed Ion Monolayer Model

A computer simulation of the dependence of $d_n(x)$ on x was carried out in order to provide a useful model for the experimental results in Fig. 15. Our model began with the definition of a transverse layer rigidity parameter " p ". Consider the single mono-layer system shown in Fig. 17 in which there is one gallery ion per host layer unit cell. If we begin with all small "B" ions in the gallery and replace one of them with a larger "A" ion, then one or more unit cells in each layer defining the gallery surfaces will undergo a distortion. The distortion of one primitive layer unit cell per "A" cation would represent an infinitely floppy host layer with a layer rigidity parameter of $p=1$. For the distortion of all unit cells ($p=\infty$), the layer would be infinitely rigid. Intermediate values of p would quantitatively describe the degree of layer rigidity. Depending on the size of the unit cell, each value of p would be associated with a characteristic healing length λ .



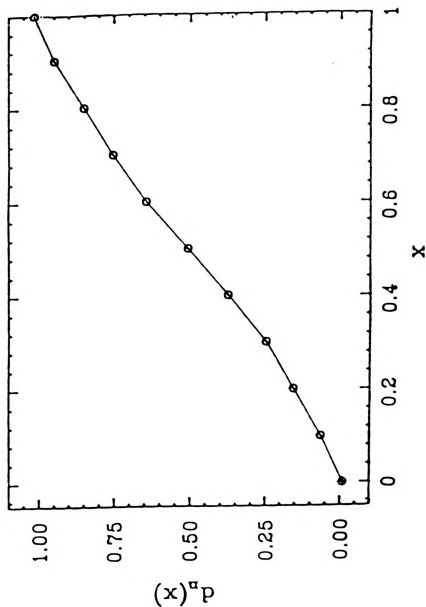


Fig. 16 The composition dependence of the normalized basal spacing for ion segregation in $[(\text{CH}_3)_4\text{N}^+x^-x^-[(\text{CH}_3)_3\text{NH}^+]_{1-x}]$ -x-vermiculites based on the Reynolds model. The basal spacings were calculated from least square regression of the first six 001 reflections.

The simulation results are shown in Fig. 17 for several different values of p for the triangular net. In the floppy layer limit where $p=1$ and the healing length $\lambda=0$, a Vegard's law behavior is obtained. However, in the infinitely rigid layer region where $p=\infty$, $\lambda=\infty$, the initial slope is infinite. For the intermediate cases: $p=7$, $\lambda=a_0$ and $p=13$, $\lambda=\sqrt{3}a_0$, there are differences in the initial slopes and in the x values at which each d_n reaches 1. Significantly, there is no percolation threshold even for finite values of p because $d_n(x)$ depends upon all of the large ions, not only on those belonging to the infinite percolation cluster.

III-4. Infrared and Raman Spectroscopies of Mixed

$[(CH_3)_4N^+]_x[(CH_3)_3NH^+]_{1-x}$ -Vermiculites

Two series of angle-dependent infrared spectra for trimethylammonium vermiculite ($x=0.0$) and for a mixed-ion $[(CH_3)_4N^+]_x[(CH_3)_3NH^+]_{1-x}$ -vermiculite with $x=0.54$ are shown in Fig. 18 and Fig. 19, respectively. In both cases, the peak intensity of the hydrogen-bonded N^+-H stretching absorption band of interlayer $(CH_3)_3NH^+$ at about 2730 cm^{-1} ,³⁴ relative to the trapped water O-H stretching at 3280 cm^{-1} ,³⁵ and the in-phase C-H stretching band at 2970 cm^{-1} and at 3040 cm^{-1} ,³⁶ increases upon decreasing the angle between sample film and the incident infrared beam. This means that the orientations of N^+-H dipoles in the galleries

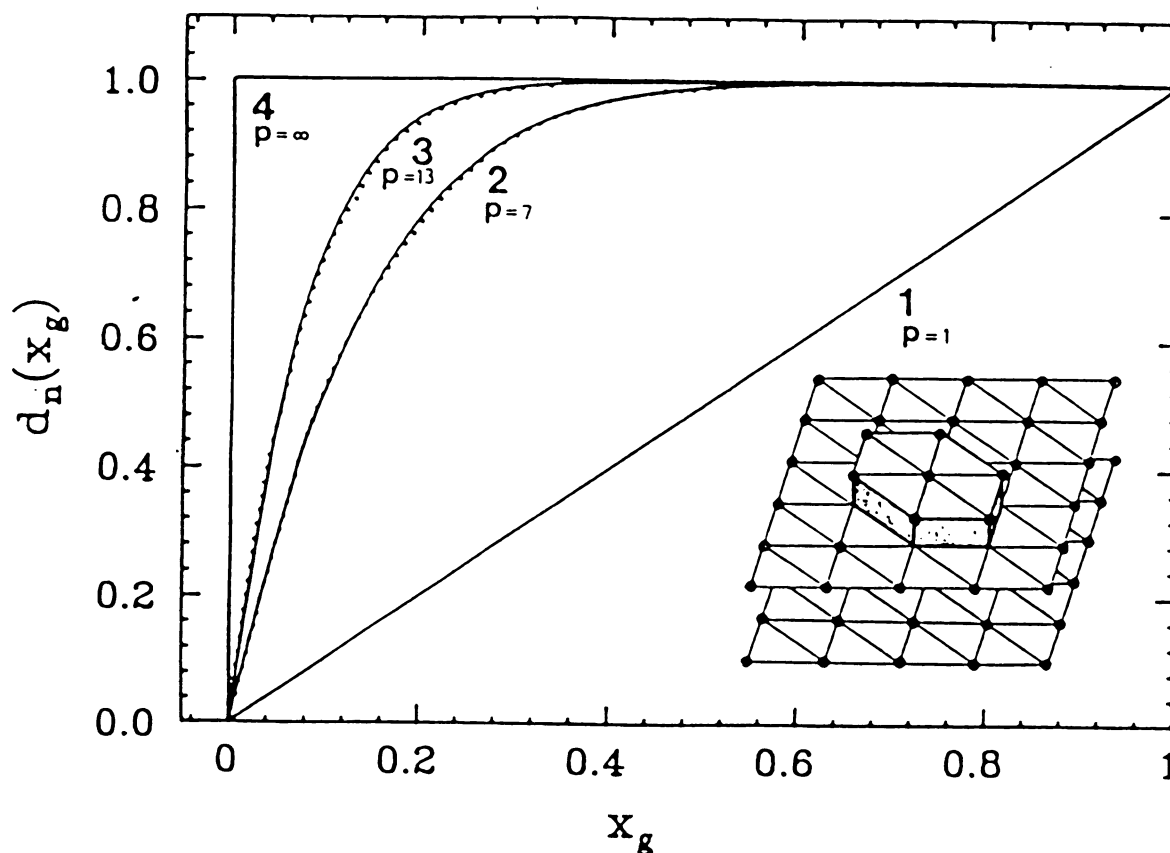


Fig. 17 Monolayer triangular lattice simulations (dotted lines) of $d_n(x)$ for idealized $[A]_x[B]_{1-x}$ vermiculites for several different values of the healing length, λ , and the layer rigidity parameter, p . The solid lines are from Equation 4 of the text with (1) $p=1, \lambda=0$; (2) $p=7, \lambda=a_0$; (3) $p=13, \lambda=\sqrt{3} a_0$; (4) $p=\infty, \lambda=\infty$. Inset: the triangular lattice defined by the spherical A and B pillaring cations. The expanded region represents the distortion which occurs in the host layer when A replaced B and $\lambda=a_0$. In this latter case, the number of expanded sites is $p=n+1=7$ where n is the number of nearest neighbors.

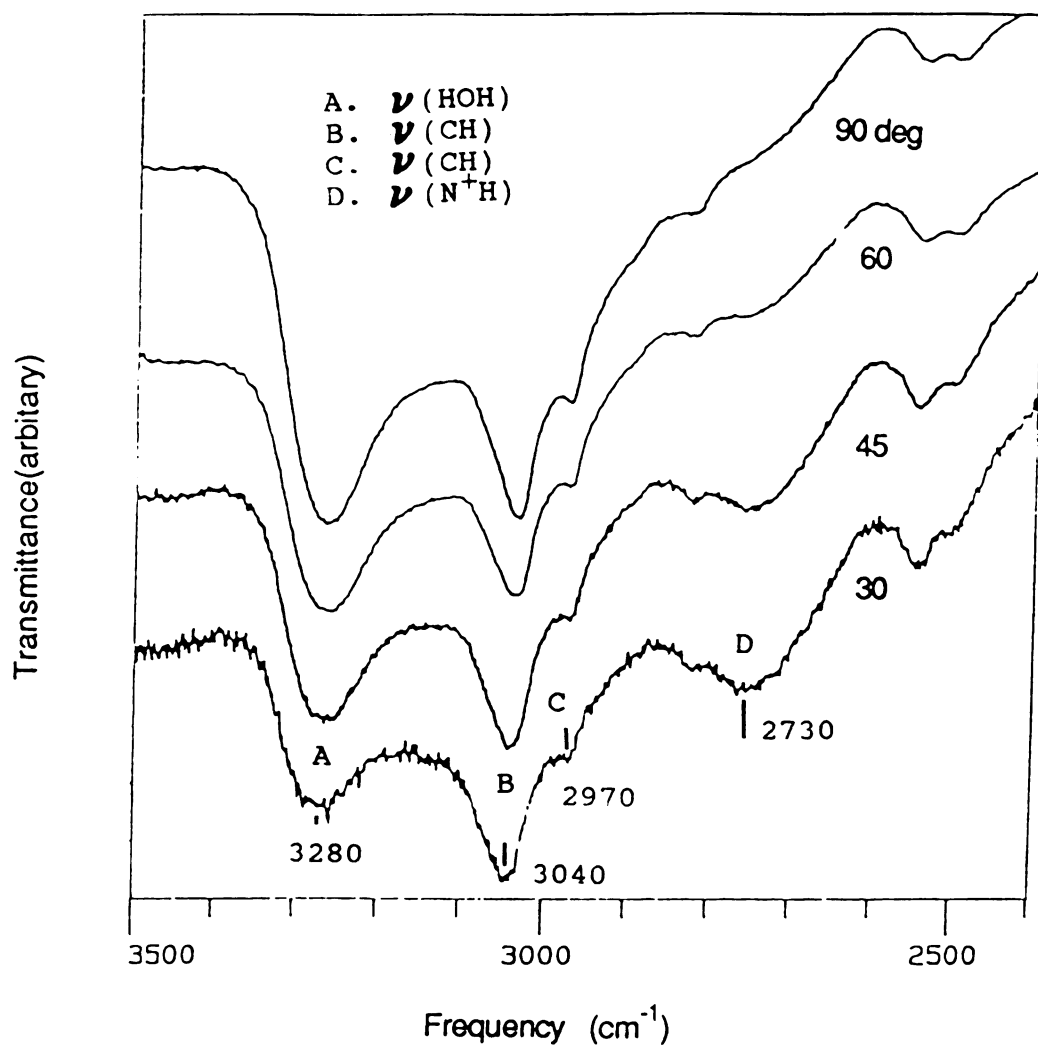


Fig. 18 IR spectra of $(\text{CH}_3)_3\text{NH}^+$ -vermiculite with different incident beam angles. Note the change in relative peak intensity of the $\text{N}^+\text{-H}$ stretching at 2730 cm^{-1} relative to other angle-independent peaks.

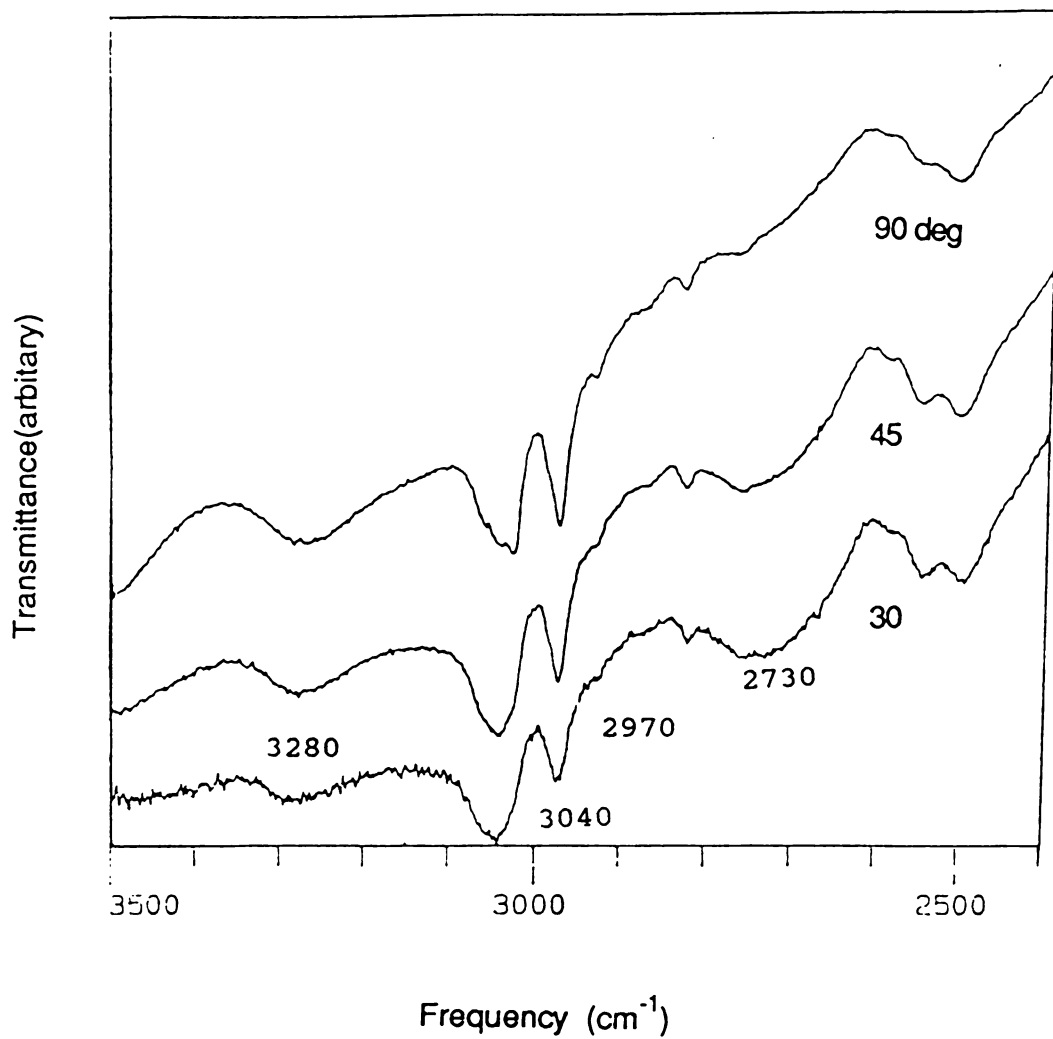


Fig. 19 IR spectra of $[(\text{CH}_3)_4\text{N}^+]_{0.54}[(\text{CH}_3)_3\text{NH}^+]_{0.46}^-$ vermiculite for different incident beam angles. Note the change in relative peak intensity of the $\text{N}^+\text{-H}$ stretching at 2730 cm^{-1} relative to other angle-independent peaks.

of samples are perpendicular to the clay layers, regardless of the interlayer ion composition.

In Fig. 20, typical room temperature low frequency Raman spectra of the $[(\text{CH}_3)_4\text{N}^+]_x[(\text{CH}_3)_3\text{NH}^+]_{1-x}$ -vermiculites are shown for different values of x . The in-plane torsional mode of the silicate layers, whose frequency and eigenvector are well known from the calculation of Ishii et al.,³² is observed at about 118 cm^{-1} . As the x value increases, the torsional mode frequency for the mixed cation vermiculite shifts non-linearly to higher frequency as shown by the plot in Fig. 21. Two distinct regions can be distinguished from the shape of the plot. In the region $0 < x < 0.25$, little or no frequency shift is observed. On the other hand, in the region $0.25 < x < 1$, there is almost a linear relationship between frequency shift and the x value.

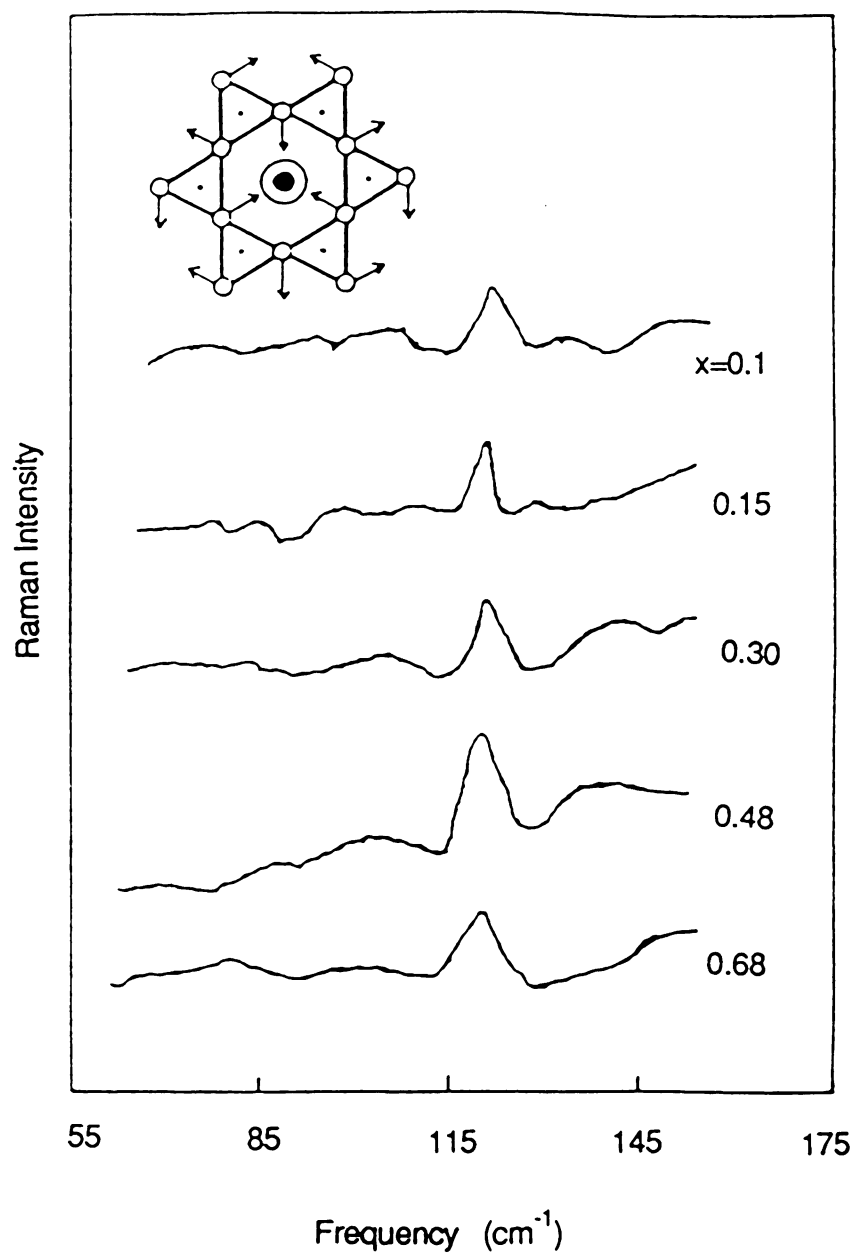
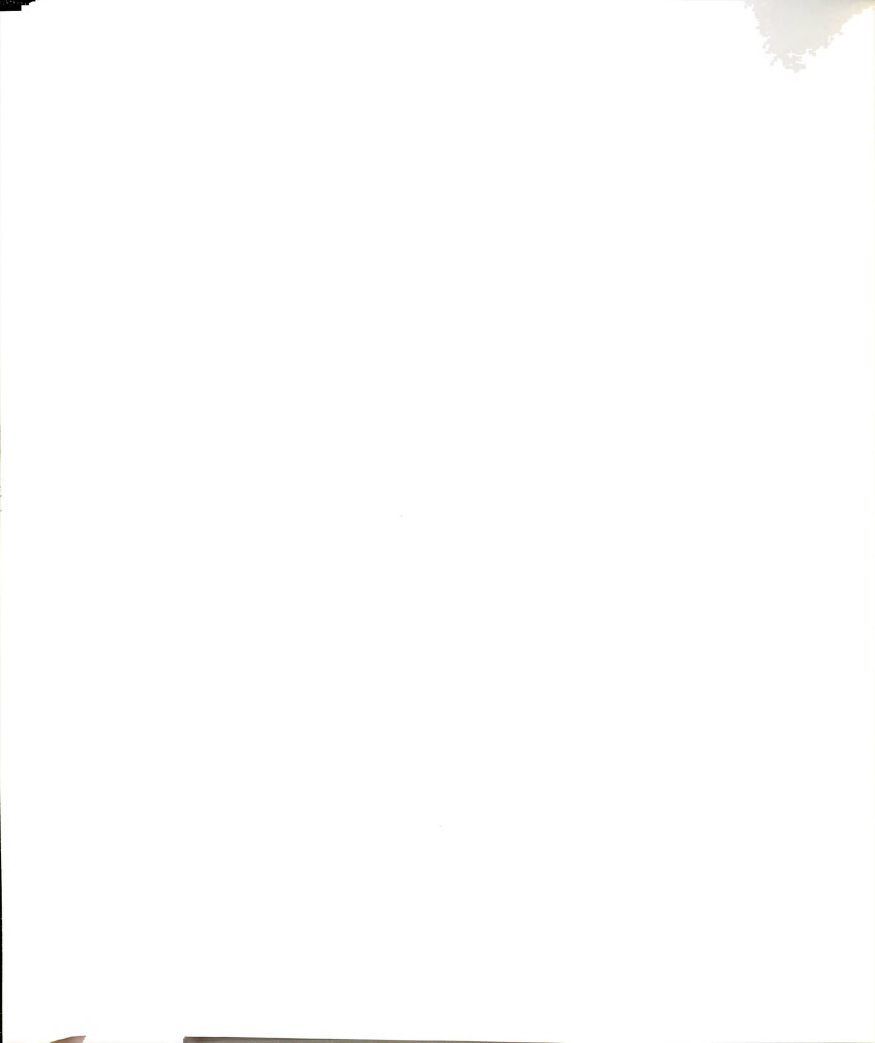


Fig. 20 Low frequency Raman spectra of $[(\text{CH}_3)_4\text{N}^+]_x[(\text{CH}_3)_3\text{NH}^+]_{1-x}$ vermiculites. The insert identifies the eigenvector of the vibration



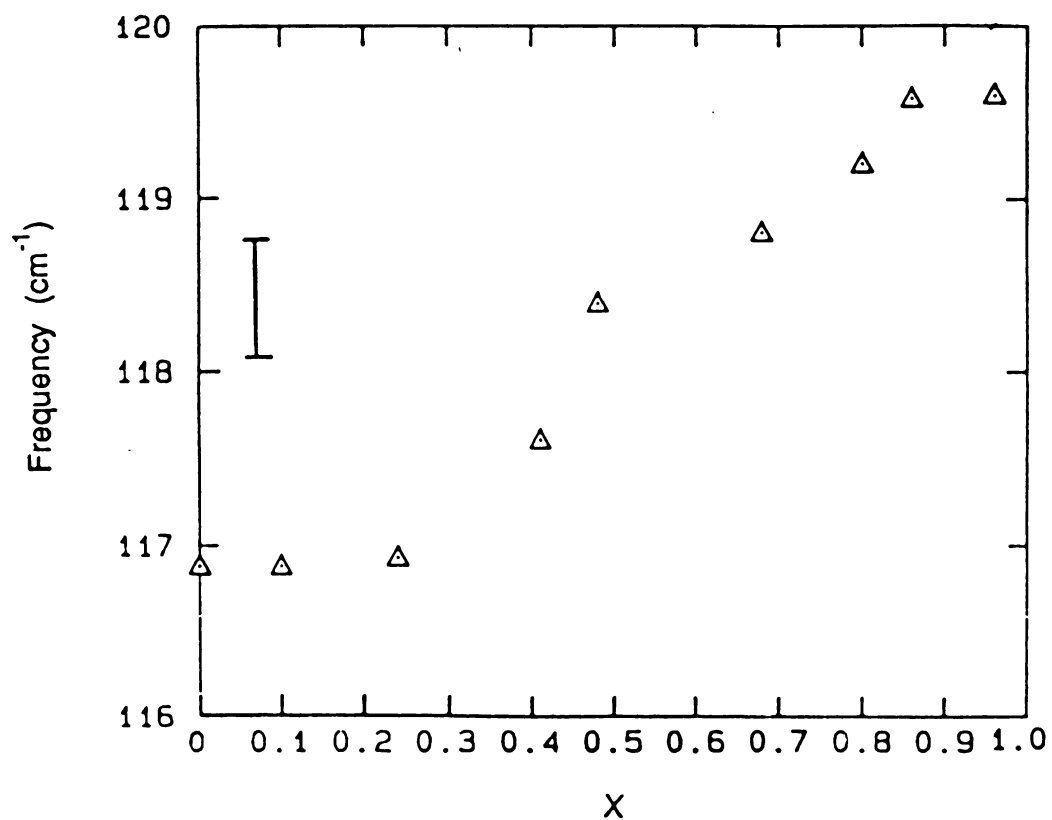


Fig. 21 X-dependence of the torsional mode frequency for $[(\text{CH}_3)_4\text{N}^+]_x[(\text{CH}_3)_3\text{NH}^+]_{1-x}$ vermiculites. The error bar indicates the uncertainty in the frequency measurements

IV. DISCUSSION

In considering different synthetic pathways to mixed ion clays for layer rigidity studies, it was realized that differences in solvation properties for the two ions could lead to segregation of the ions into separate galleries, as other researchers reported.^{37,38,39} Such ion-segregated-interstratified clays would be of no value in addressing the layer rigidity issue. For this reason we developed a synthetic strategy which allowed us to control the gallery exchange ion distribution by moderating reaction kinetics rather than allowing thermodynamic factors to determine the final gallery ion distribution.

The key to the successful synthesis of mixed $[(\text{CH}_3)_4\text{N}^+]_x[(\text{CH}_3)_3\text{NH}^+]_{1-x}$ -vermiculite was the difference in labilities of the homo-ionic $(\text{CH}_3)_3\text{NH}^+$ - and $(\text{CH}_3)_4\text{N}^+$ -vermiculites. The $(\text{CH}_3)_3\text{NH}^+$ derivative undergoes extensive exchange ion solvation and, consequently, the swollen galleries are readily accessible for ion exchange reaction. In contrast, the galleries of the $(\text{CH}_3)_4\text{N}^+$ derivative are only partially solvated by water. So, the layers remain in face-to-face association and ion exchange reaction is slow. Thus, when $(\text{CH}_3)_3\text{NH}^+$ -vermiculite in aqueous suspension is allowed to react with controlled amounts of $(\text{CH}_3)_4\text{N}^+$, the partial replacement of $(\text{CH}_3)_3\text{NH}^+$ by $(\text{CH}_3)_4\text{N}^+$ leads to the

flocculation of the clay and the entrapment of both ions within the galleries. Redistribution of the ions into segregated galleries is inhibited by the limited swelling and reduced lability of the gallery regions.

The relative inertness of vermiculite-intercalated $(\text{CH}_3)_4\text{N}^+$ ions toward ion exchange is further manifested in the formation of two distinct homo-ionic phases upon reaction of Mg-vermiculite with excess $(\text{CH}_3)_4\text{N}^+$ ions. Although initial reaction up to approximately 10 % exchange is quite facile, the exchange rate diminishes rapidly with increasing extent of exchange. We attribute the formation of a pure $(\text{CH}_3)_4\text{N}^+$ -vermiculite phase at the initial stages of reaction to the replacement of magnesium ions near the layer edges. As the edge sites become saturated, the propagation of the exchange front across a gallery is inhibited by the strong binding and kinetic inertness of the $(\text{CH}_3)_4\text{N}^+$ ion on the gallery surfaces. In contrast, the rate of the replacement of magnesium ions by $(\text{CH}_3)_3\text{NH}^+$ ions is approximately 2 times faster than for $(\text{CH}_3)_4\text{N}^+$ case. The faster exchange reaction exchange is facilitated by the swelling of the galleries of the trimethylammonium vermiculite.

Evidence for the uniform mixing of alkylammonium ions in $[(\text{CH}_3)_4\text{N}^+]_x[(\text{CH}_3)_3\text{NH}^+]_{1-x}$ -vermiculite is provided by three independent experimental results:

1. The observed intensities and positions of the 001 reflections are in accord with those predicted from

structure factor calculations for an intercalate with a solid solution arrangement of ions in galleries of uniform height.

2. The two randomly interstratified models, namely the Hendricks-Teller model and the Reynolds model, in which the two different kinds of alkylammonium ions are segregated into separate galleries of differing heights, predict 001 positions that are in poor agreement with those observed. In addition, the shape of the $d_n(x)$ vs x plot for the experimental mixed ion system is totally different from that of the randomly interstratified Reynolds model system.

3. A direct Fourier transform of the one dimensional xrd pattern, the so-called one-dimensional Patterson synthesis, did not show signs of interstratification. Also, the observed Q vs l plots for the experimental mixed ion system are linear within experimental uncertainty.

Our monolayer simulation model provides valuable insights into the anticipated behavior of gallery height expansion as the smaller ions are replaced by larger ions in a mixed ion system. Our model assumes that all positions of the Kagome net on the gallery surfaces are occupied by an exchange cation. In fact, 86% of the hexagonal cavities are occupied by alkylammonium ions in our experiments. Thus, the exchange cations only approximate a triangular lattice. Nevertheless, the general features contained in our model are realized for the mixed ion vermiculite. In particular, an abrupt increase in $d_n(x)$ is expected upon replacing the

smaller pillaring ions with larger pillaring ions. Such an abrupt increase in $d_n(x)$ is indeed observed, but it is preceded by a sub-linear threshold region in which there is little or no dependence of $d_n(x)$ on x (cf., Figure 15). This threshold behavior is outside of the monolayer model.

There are two possible mechanisms which may give rise to the threshold behavior of $d_n(x)$ for the $[(CH_3)_4N^+]_x - [(CH_3)_3NH^+]_{1-x}$ -vermiculite. Firstly, at the early stages of replacement of the smaller alkylammonium ion ($x=0-0.2$) the ions may segregate into separate galleries, but uniform mixing of ions may occur at higher values of x ($x>0.20$). However, this x -dependent ion segregation mechanism is unlikely because there is no apparent reason why the mixed ion system should be segregated at low values of x and uniformly mixed at high values of x , especially when dealing with single-crystal vermiculite wherein the layer charge is expected to be more or less uniform.

The second possible mechanism invokes the presence of two types of ion-binding sites. One site is the gallery positions already defined in our monolayer model. In addition, however, there may be ion exchange positions, such as the edges of the clay platelets, which do not contribute to or influence the observed gallery heights. Such sites, which are independent of x , and which do not contribute to the magnitude of $d_n(x)$, shall be referred to as "defect sites." The threshold in the $d_n(x)$ vs x plots can then be explained qualitatively by the preferential binding of

$(\text{CH}_3)_4\text{N}^+$ ions at the defect sites. Once the defect sites are saturated near a threshold value(x_t) of $x=0.2$, the further addition of $(\text{CH}_3)_4\text{N}^+$ ions results in the abrupt expansion of the gallery region. This second mechanism seems to be much more plausible than the bimodal ion-segregation/ion-mixing mechanism described earlier.

We now consider a quantitative treatment of transverse layer rigidity in our alkylammonium pillared clay while at the same time allowing for the binding of pillaring ions at both ordered gallery sites and defect sites. We assume the basal spacing to be dependent on the gallery $(\text{CH}_3)_4\text{N}^+$ ion concentration x_g . The latter quantity is a function of the total $(\text{CH}_3)_4\text{N}^+$ composition x . The dependence x_g on x is determined by two parameters, f and Δ/kT where $f=N_d/N_g$ is the fraction of the defect sites relative to the gallery sites and Δ is the effective binding energy difference between these two sites. The binding of $(\text{CH}_3)_4\text{N}^+$ ions should be favored over $(\text{CH}_3)_3\text{NH}^+$ ions at the defect sites, owing to the larger volume of such sites. For simplicity, we assume only one type of defect site.

A statistical mechanical calculation⁴⁰ relates x_g to x , f , Δ/kT . The steps involved in the calculations are described in Appendix III. Basically, $(\text{CH}_3)_4\text{N}^+$ cations are treated as the particles which follow the Fermi distribution function for the distributions of $(\text{CH}_3)_4\text{N}^+$ cations in both sites. The result is Equation 5, which relates x_g to x :



$$x = \frac{1}{1+f} x_g + \frac{f}{1+f} \left(\frac{1}{1 + \left(\frac{1}{x_g} - 1 \right) e^{-\Delta/kT}} \right) \quad (5)$$

From this relationship we expect that for $x < x_t$, the $(\text{CH}_3)_4\text{N}^+$ ions preferentially occupy the defect sites characterized by the parameters f and Δ/kT . For a given x , the preferential binding of the large ion at defect sites will reduce the gallery $(\text{CH}_3)_4\text{N}^+$ ion concentration and yield a sublinear increase in $d_n(x)$. For $x > x_t$, additionally ingested $(\text{CH}_3)_4\text{N}^+$ ions enter the galleries and the result is a rapid increase in $d_n(x)$.

On the basis of methods recently developed by Xia and Thorpe,⁴¹ the analytical solution shown in Equation (6), can be obtained for our monolayer simulation model:

$$d_n(x_g) = [1 - (1 - x_g)^p] \quad (6)$$

$$x_g = \Phi(x, f, \Delta/kT)$$

Here, $p=n+1$, the total number of sites expanded by the larger ion exchange in the gallery and n is the number of layer triangular sites that are transversely puckered by the insertion of a large cation. The p parameter, which is approximately proportional to the square of the healing

length, is defined as the transverse layer rigidity parameter in the monolayer model.

Equation 6 fits the simulated monolayer model extremely well, as shown by the solid lines in Figure 17 for four different sets of transverse layer rigidity parameters. No percolation threshold is predicted for $d_n(x)$ in this case because all of the pillaring ions occupy gallery sites which directly influence the gallery heights. Equation 6 may be readily adapted to a two-site binding model in which one site is a defect site which does not contribute to the gallery height of the mixed ion clays and the second type of site is a gallery site. By substitution of x_g in Equation 6 using Equation 5, we can express x_g in terms of the overall composition x , the ratio of defect to gallery sites f , and the binding energy difference between the two sites Δ . Hence, Equation 6 takes the form shown in Equation 7.

$$d_n(x) = [1 - \{1 - \Phi(x, f, \Delta/kT)\}^p] \quad (7)$$

We have used Equation 7 to obtain a non-linear least-squares-fit to the data of Figure 15. The parameters which gave the best fit (solid line in Figure 15) are $p=8.0$, $f=0.5$, $\Delta/kT=4.3$. Despite the limitations of our monolayer model, particularly the abruptness of the layer distortions in the vicinity of the large ion positions, the parameters obtained for the best least-squares-fit are physically plausible. The difference in binding energy for the two binding sites amounts to only about 2.5 Kcal/mole. The value of the layer rigidity parameter $p=8.0$ indicates that little or no transverse layer distortion occurs at lateral distances up to one unit cell from the pillar position, which in our model is about 5.3 Å. This means that "sagging" does not occur at cell positions adjacent to the pillaring site, and that the galleries remain fully expanded when two pillars are separated by a distance of at least 10.6 Å.

The f value of 0.5 indicates that 33% of the exchange cations are at positions other than those which contribute to the observed basal spacings. It is instructive here to consider the possible defect sites other than edge sites which do not contribute to the observed basal spacings. In our synthetic procedures, the clay layers are initially in a greatly swollen state due to unique swelling property of the trimethylammonium exchange form. When the layers are reflocculated by the addition of tetramethylammonium ions, several types of defect centers may be introduced. Fig. 22 illustrates possible defect sites for exchange ions on basal

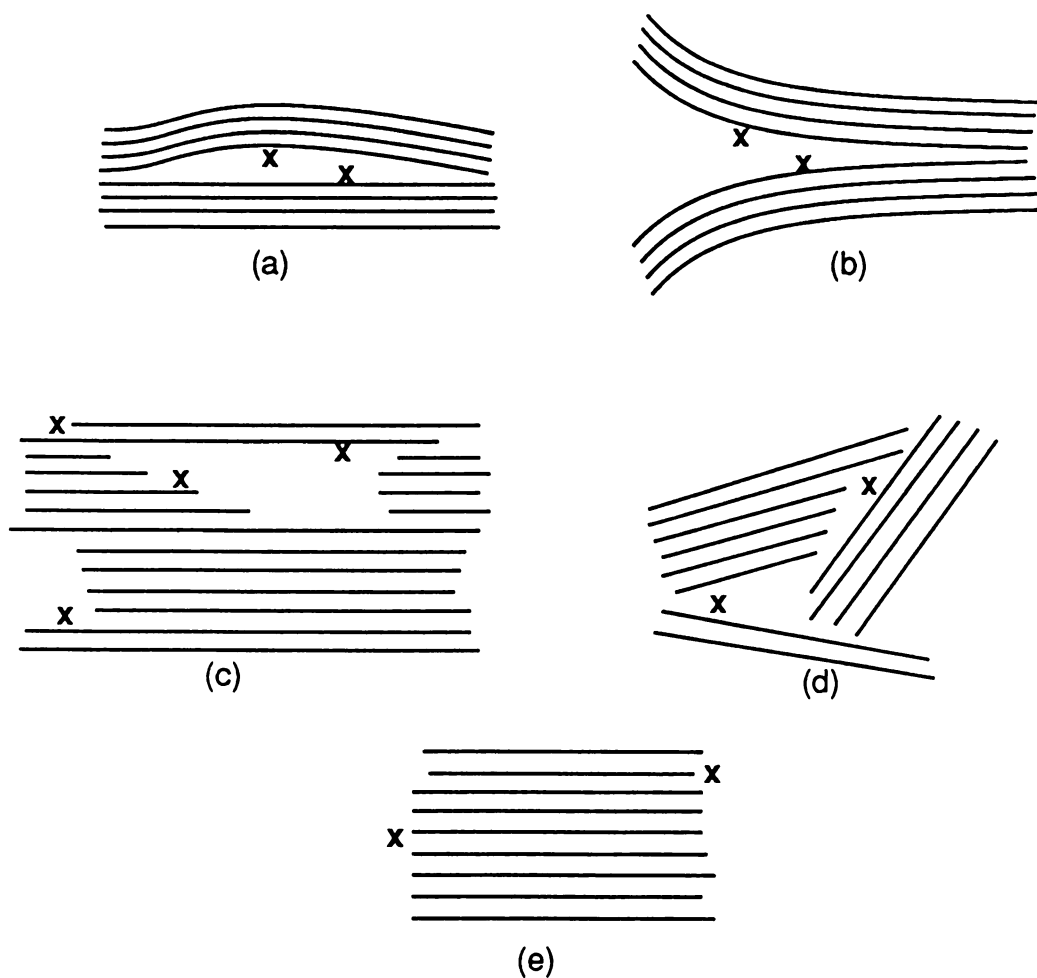


Fig. 22 Schematic illustration of possible non-gallery defect sites for exchange ions on the basal surfaces (designated x) which do not contribute to the 001 basal spacing
 (a): Surfaces at twisted layer-planar layer interfaces, (b): Surfaces of bifurcated layers, (c): Surfaces of internal and external ledges and crevices formed by layer termination, (d): Surfaces of layer edge-layer face interfaces. Defects (a)-(d) are in addition to non-gallery binding sites at layer edges(e)

surfaces in reconstituted alkylammonium vermiculite tactoids. The surfaces marked by an "x" indicate the positions of the pillaring cations on basal surfaces which do not contribute to the basal spacing change. In addition to the basal positions formed by these four different types of defects, the exchange ions can occupy positions at the edges of the layers which also do not contribute to the basal spacing. Thus there is a large variety of possible defect sites in pillared clays. High resolution electron microscopy studies are currently underway in an effort to identify such non-gallery defects.

In Fig. 23, the calculated gallery site concentration of $(\text{CH}_3)_4\text{N}^+$ is plotted against the total $(\text{CH}_3)_4\text{N}^+$ concentration. As expected, there are two regions in x_g vs. x curve. For the low x value range, the $(\text{CH}_3)_4\text{N}^+$ cations prefer defect sites, which results in a small increase of x_g . Beyond a certain x value, an almost linear relationship is observed between x_g and x . The initial small increase in the large cation concentration in the gallery sites results in the rapid increase of d -spacing due to a finite layer rigidity, as described by the simulation results.

The infrared and Raman spectroscopy studies on the mixed $[(\text{CH}_3)_4\text{N}^+]_x[(\text{CH}_3)_3\text{NH}^+]_{1-x}$ -vermiculites (cf., Figure 18-21) also provided insight into the mixed ion systems. The orientation of smaller cations in the gallery affects the apparent height of the trimethylammonium cation and, also, the d -spacing of the clay. The orientation of $\text{N}^+\text{-H}$ dipoles

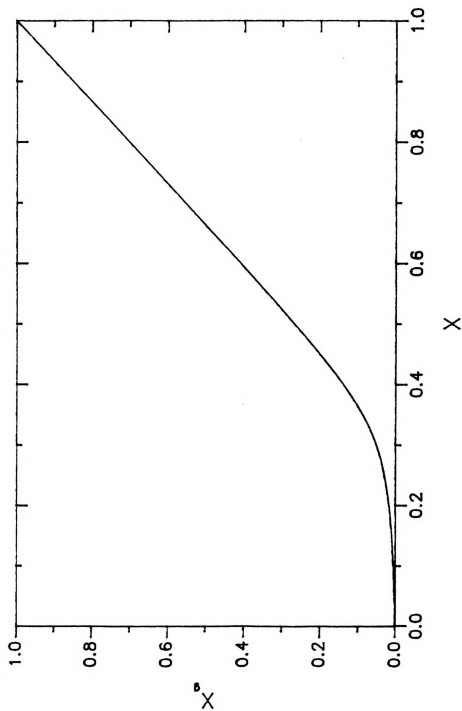


Fig. 23 Plot of the dependence of gallery ion composition x_g on the total $(\text{CH}_3)_4\text{N}^+$ composition x for $[(\text{CH}_3)_4\text{N}^+]_x[(\text{CH}_3)_3\text{NH}^+]_{1-x}$ -vermiculites. The two binding site model assumes $p=8$, $f=0.5$, and $\Delta/kT=4.3$.

of trimethylammonium ions in vermiculite galleries was determined to be perpendicular to the oxygen planes of layer, regardless the ratios of the two different cations. The specific orientation of the trimethylammonium cations in the gallery is probably attributed to the dominant van der Waals interaction between the three methyl groups and the surface oxygen atoms, in addition to hydrogen bonding between N^+-H and basal oxygen atoms. Such a specific orientation of smaller cations in the galleries satisfies the requirement of our monolayer model in defining the sizes of cations.

The Raman shifts for the torsional mode of the surface oxygen planes in mixed $[(CH_3)_4N^+]_x[(CH_3)_3NH^+]_{1-x}$ -vermiculite are well correlated with the two different cation sites of our mixed ion clay model. A comparison of x_g vs. x plot (Fig. 23) with the plot of Raman shift vs. x (Fig. 21) clearly shows the dependency of Raman shift on x_g , the gallery $(CH_3)_4N^+$ concentration.

Qualitatively, the Raman shift of the torsional mode can be related with the collective interactions between the interlayer cation and hexagonal oxygen atoms during the vibration. Apparently, the concentration increase of the larger $(CH_3)_4N^+$ cation in the gallery results in a linear increase in the extent of the interactions. In the range of $x < 0.25$ in Fig. 21, there is almost no change in the Raman frequency, which might be due to the defect site effects for the real vermiculite samples. Also, in the range of $0.25 < x$

< 1.0 , a linear increase in Raman frequency is observed with increasing the x value. This latter dependence can be interpreted in terms of a linear increase in the x_g value, as calculated from the two site model parameters (cf. Fig. 23).

V. CONCLUSIONS

The major conclusions of this study are as follows:

1. Mixed ion clay systems $[(\text{CH}_3)_4\text{N}^+]_x[(\text{CH}_3)_3\text{NH}^+]_{1-x}$ - vermiculites have been prepared which are suitable for quantitatively describing the transverse layer rigidity of host silicate layers by observing the relationship between gallery height and the fraction of pillaring $(\text{CH}_3)_4\text{N}^+$ ion occupying the gallery surfaces.

2. A layer rigidity parameter ($p=8$) for vermiculite host layers was determined by analytical and two-site ion binding model simulation. This model now makes it possible to quantitatively compare the transverse layer rigidities of several different types of host systems and to explicitly determine the structural and compositional factor influencing the pillaring of lamellar solids.

Appendix I

A. Calculation of the One-Dimensional (00 ℓ) X-Ray Diffraction Pattern for [(CH₃)₃NH⁺] -Vermiculite

$$1. \text{ Intensity } (\theta) = K * LP(\theta) * |G(\theta)|^2 * \Phi(\theta)$$

K : constant

LP : the Lorentz Polarization factor

Lorentz factor : Instrument and geometry
dependent

Polarization factor : due to polarized X-ray
scattering

|G(θ)|² : square of structure factor of unit cell

Φ : Interference function

2. LP factor calculation

$$LP = \frac{(1 + \cos^2 2\theta) \Psi}{\sin 2\theta}$$

Ψ : powder ring distribution factor

for a random powder :

Ψ is proportional to $\frac{1}{\sin \theta}$

for a single crystal :

Ψ is a constant

for a clay sample :

Ψ is intermediate

Reynolds method⁴² is used
to calculate Ψ

3. One-dimensional structure factor calculation

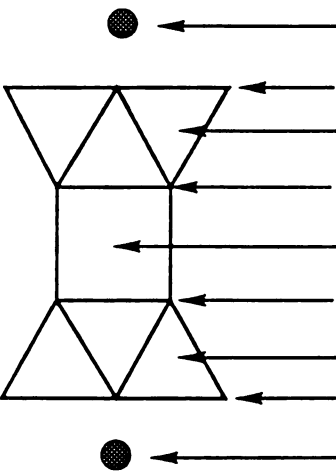
$$G = \sum_{\text{plane}} n f (\cos (RQ) + i \sin (RQ))$$

n : number of like atoms in a plane

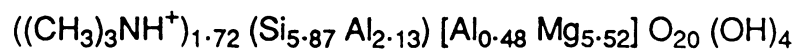
$f(\theta)$: atomic x-ray scattering factor

R : distance from origin

$$Q : \frac{4\pi \sin \theta}{\lambda}$$

	$R \text{ (Å)}$	$\Sigma n \cdot \text{atom/plane}$
	6.35	0.86 $(\text{CH}_3)_3\text{NH}^+$
	3.295	6.00 O
	2.77	2.94 Si + 1.06 Al
	1.07	4.00 O + 2 (OH^-)
	0	0.48 Al + 5.52 Mg
	-1.07	4.00 O + 2 (OH^-)
	-2.77	2.94 Si + 1.06 Al
	-3.295	6.00 O
	-6.35	0.86 $(\text{CH}_3)_3\text{NH}^+$

Unit cell formula :



4. Interference function $\Phi(\theta)$

$$\Phi(\theta) = N/2 + \sum_{n=1}^{N-1} (N-n) \cos(QR_s)$$

N : number of layers per crystal

R_s : the distance between diffraction layers
within which diffraction is considered

$$Q : \frac{4\pi \sin \theta}{\lambda}$$

In Fig. 24, the 2θ dependent LP factor, the square of structure factor, the interference function, and the $00l$ intensities of the calculated xrd pattern for $(\text{CH}_3)_3\text{NH}^+$ - vermiculite are shown.

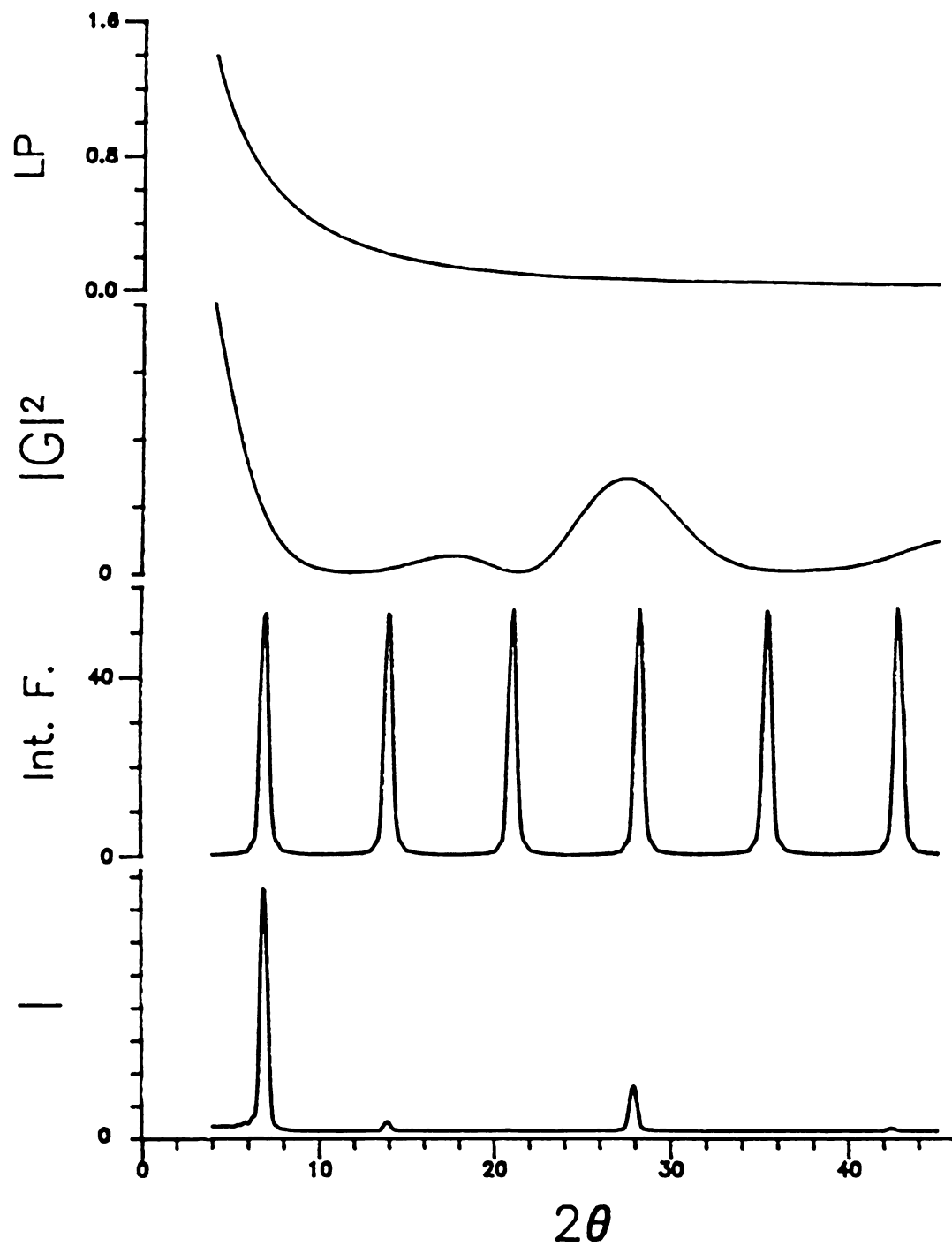
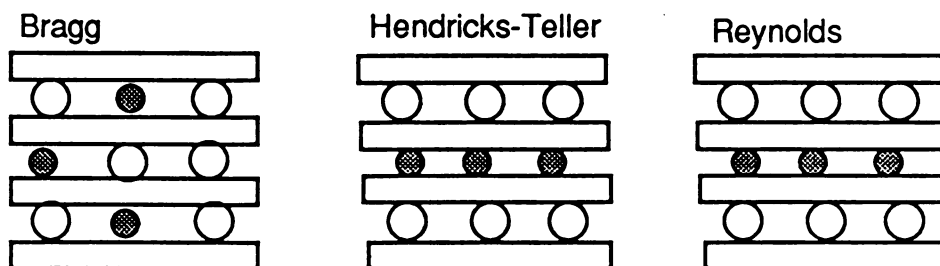


Fig. 24 2θ dependence of the LP factor, squared structure factor, interference function, and intensity in the xrd pattern calculation of $(\text{CH}_3)_3\text{NH}^+$ -vermiculite

B. Basis for the Bragg, Hendricks-Teller and Reynolds Models



Layer parameters

1. 5 - 15 layers stacking	Infinite	5 - 15 layers stacking
2. Linear distribution of stacked layer thicknesses	not applicable	Linear distribution of stacked layer thicknesses
3. $(\text{CH}_3)_3\text{NH}^+$ - Vermiculite structure factor	$(\text{CH}_3)_3\text{NH}^+$ - Vermiculite structure factor	$(\text{CH}_3)_3\text{NH}^+$ - Vermiculite structure factor and $(\text{CH}_3)_4\text{N}^+$ - Vermiculite structure factor
4. a single d-spacing from expt.	12.70 and 13.34 Å d-spacings as end members	12.70 and 13.34 Å d-spacings as end members
5. Regular sequence	Random sequence of two different unit layers	Random sequence of two different unit layers

LP factor

Reynolds' modified LP factor was used for all calculations



Equations for the calculation 00/ reflections Based on Bragg,
Hendricks-Teller and Reynolds Models

Bragg

$$I = LP |G|^2 \times \left(N/2 + \sum_{n=1}^{N-1} (N-n) \cos(QR_s) \right)$$

where

LP: Lorentz Polarization factor

$|G|^2$: square of structure factor of unit cell

N : number of layers per crystal

R_s : the distance between layers

diffraction is considered

$$Q : \frac{4\pi \sin \theta}{\lambda}$$

Hendricks-Teller

$$I = \frac{LP |G|^2 \times P_A P_B \sin^2(Q/2 [D_A - D_B])}{1 - P_A P_B \sin^2(Q/2 [D_A - D_B]) - P_A \cos(QD_A) - P_B \cos(QD_B)}$$

P_A : proportion of species A

P_B : proportion of species B

D_A : thickness of A layer

D_B : thickness of B layer

Reynolds

$$I = LP \sum_S G_j^* G_k \alpha_s (\cos QS + i \sin QS)$$

S : value of a spacing considered

α_s : frequency of occurrence of S spacing

G_j, G_k : structure factor of layers

Appendix II

If we follow the results of the two site monolayer model, x_g (gallery site $(\text{CH}_3)_4\text{N}^+$ concentration) is different from x in $[(\text{CH}_3)_4\text{N}^+]_x[(\text{CH}_3)_3\text{NH}^+]_{1-x}$ - vermiculite due to the non-gallery defect site contributions.

Therefore, x_g rather than x should be used for the x-ray diffraction calculation. For $x=0.63$, $x_g=0.45$ was determined from Eq. 5 with the simulated parameter values.

To check the validity of our argument in favor of a uniformly mixed ion system, one-dimensional xrd patterns were generated using the x_g value of 0.45 rather than a value of 0.63.

In Fig. 25 and 26, the Hendricks-Teller and Reynolds patterns are compared with the experimental pattern, respectively. The Bragg pattern for x_g is the same as the pattern obtained for $x=0.63$ because the d-spacing and structure factor is independent from interlayer cation composition.

The Hendricks-Teller and Reynolds xrd patterns for demixing of ions show even greater deviations from the peak positions and shapes of the observed pattern when $x_g=0.45$ than $x=0.63$. This result further verifies our conclusions that the ions are randomly mixed within the galleries and not segregated into separate galleries.



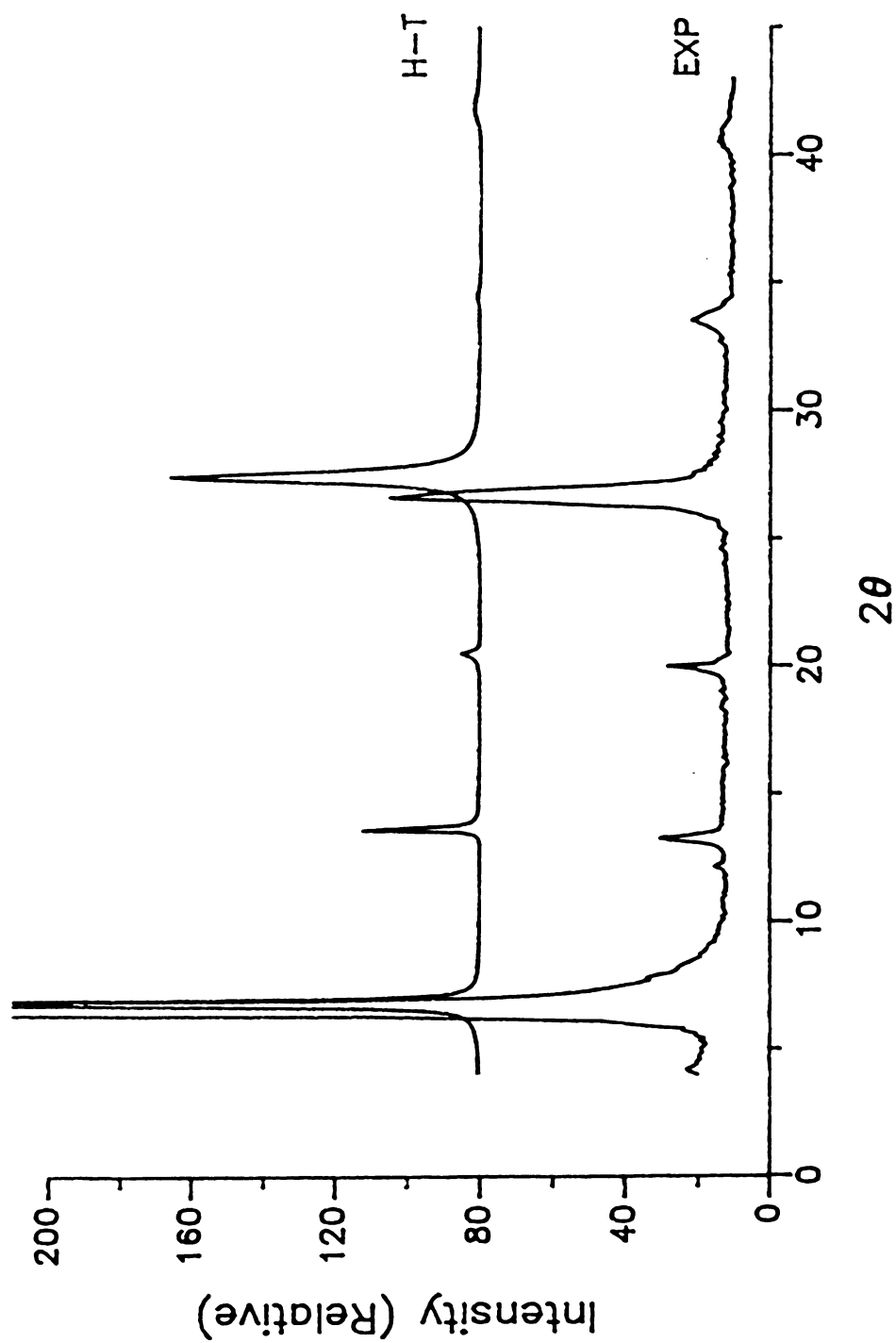
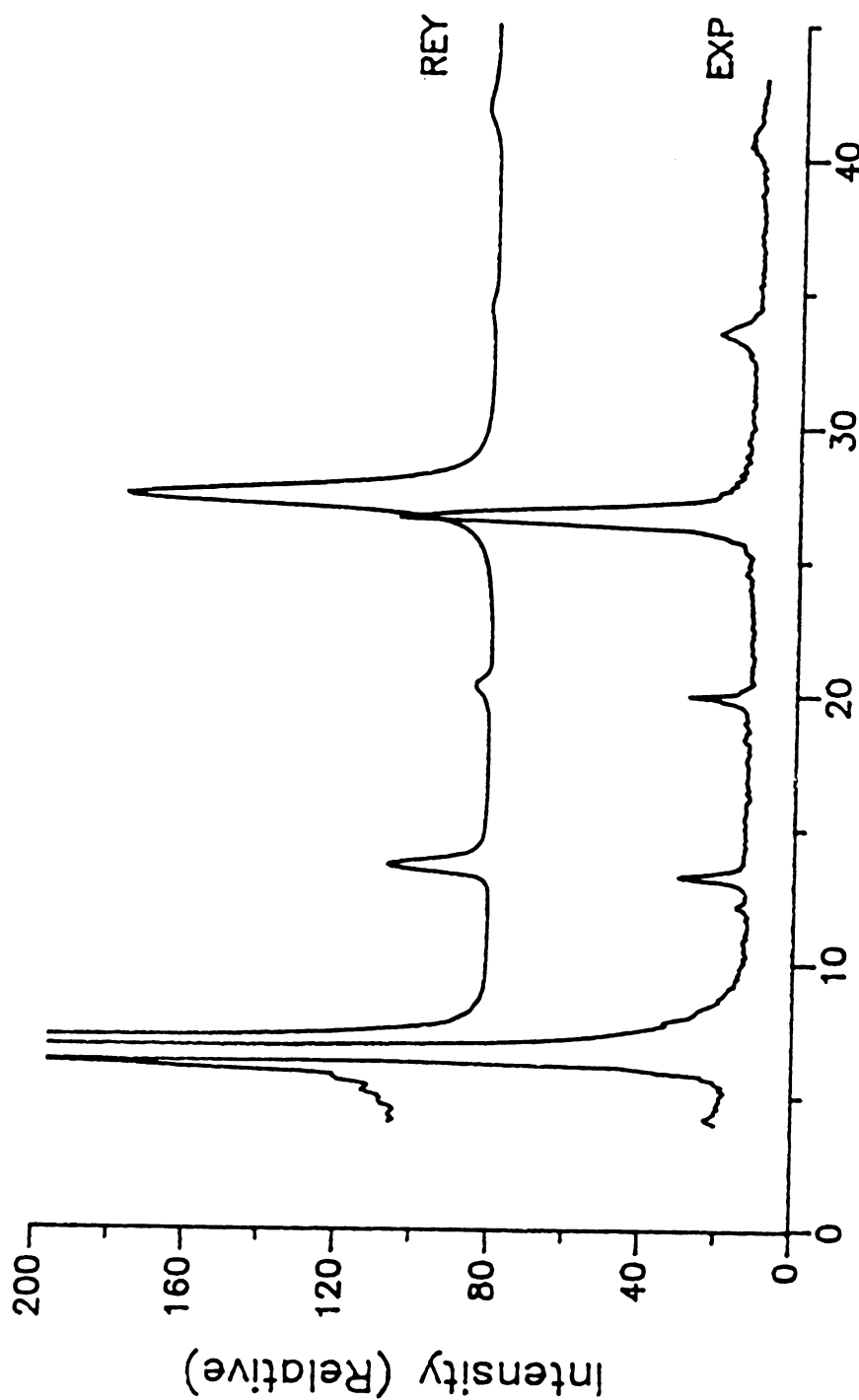


Fig. 25 Comparison of observed and calculated
 xrd patterns for $[(\text{CH}_3)_4\text{N}^+]_{0.63}$
 $[(\text{CH}_3)_3\text{NH}^+]_{0.37}$ - vermiculite using $x_g = 0.45$
 H-T : Hendricks-Teller calculation
 EXP.: Observed xrd pattern



2θ

Fig. 26 Comparison of observed and calculated
xrd patterns for $[(\text{CH}_3)_3\text{NH}^+]_{0.37}[(\text{CH}_3)_4\text{N}^+]_{0.63}$
vermiculite using $x_g=0.45$
REY : Reynolds calculation
EXP.: Observed xrd pattern

Appendix III

Derivation of Equation 5

We start with the general expression for thermodynamic potential

$$\Omega_k = -kT \log \sum [e^{(\mu - \epsilon_k)/kT}]^{n_k}$$

Ω_k : Thermodynamic potential of k^{th} level

μ : Chemical potential of particle

ϵ_k : Binding energy of k^{th} level

n_k : # of particles in the k^{th} level

For the sites that have only two choices : non occupying or occupying by a particle :

$$n_k = 0 \text{ or } 1$$

$$\Omega_k = -kT \log [1 + e^{(\mu - \epsilon_k)/kT}]$$

$$\begin{aligned} \bar{n}_k &= - \frac{d \Omega_k}{d \mu} = \frac{e^{(\mu - \epsilon_k)/kT}}{1 + e^{(\mu - \epsilon_k)/kT}} \\ &= \frac{1}{1 + e^{(\epsilon_k - \mu)/kT}} \end{aligned}$$

\bar{n}_k : Normalized # of occupancy

For the two site model :

x_g : gallery "A" ion concentration

x_d : non - gallery "A" ion concentration

ϵ_g : binding energy of gallery site

ϵ_d : binding energy of non-gallery site

Δ : $\epsilon_g - \epsilon_d$

N_d : number of non-gallery sites

N_g : number of gallery sites

f : N_d / N_g

$$x_g = \frac{1}{1 + e^{(\epsilon_g - \mu) / kT}}$$

$$x_d = \frac{1}{1 + e^{(\epsilon_d - \mu) / kT}}$$

$$x = \frac{1}{1+f} x_g + \frac{f}{1+f} x_d$$

$$= \frac{1}{1+f} x_g + \frac{f}{1+f} \left(\frac{1}{1 + e^{(\epsilon_d - \mu) / kT}} \right)$$

$$= \frac{1}{1+f} x_g + \frac{f}{1+f} \left(\frac{1}{1 + e^{(\epsilon_d - \epsilon_g + \epsilon_g - \mu) / kT}} \right)$$

$$= \frac{1}{1+f} x_g + \frac{f}{1+f} \left(\frac{1}{1 + \left(\frac{1}{x_g} - 1 \right) e^{-\Delta / kT}} \right)$$

$x_g = \Phi (x, f, \Delta / kT)$

References

1. Bailey, S. W. In *Crystal Structures of Clay Minerals and Their X-ray Identification*; Brindley, G.W.; Brown, G., Eds.; Mineralogical Society: London, 1984; p 1.
2. Theng, B. K. G. *The Chemistry of Clay-Organic Reaction*; Wiley: New York, 1974.
3. Dixon, J. B. In *Minerals in Soil Environments*; Dixon, J. B.; Weed, S. B., Eds.; Soil Science of America: Madison, 1977.
4. Mott, C. J. B. *Catalysis Today* **1988**, 2, 199.
5. Geise R. F. *Clays Clay Miner.* **1975**, 23, 165.
6. Thomas J. M. In *Intercalation Chemistry*; Whittingham M. S.; Jacobson A. J., Eds.; Academic Press: New York, 1982.
7. Vaughan E. E. W. *Catalysis Today* **1988**, 2, 187.
8. Barrer R. M.; MacLeod D. M. *Trans. Faraday Soc.* **1955**, 51, 1290.
9. Vaughan D. E. W. In *Perspectives in Molecular Sieve Science*; Flank W. H.; Whyte T. E., Eds.; American Chemical Society: Washington, 1988.
10. Barrer R. M. In *Zeolites and Clay Minerals as Sorbents and Molecular Sieve*; Academic Press: New York, 1978.
11. Pinnavaia T.J. *Science* **1983**, 220, 365.
12. Lahav N.; Shauli U.; Shabtai J. *Clays Clay Miner.* **1978**, 26, 107.

13. Yamanaka S.; Brindley G. W. *Clays Clay Miner.* **1978**, 26, 21.
14. Tzou M. S. *Ph.D Thesis*, Michigan State Univ., 1983.
15. Pinnavaia T. J.; Tsou M. S.; Landau S. D.; Raythatha R. H. *J. Molecular Catal.* **1984**, 27, 195.
16. Sterte J. *Clays Clay Miner.* **1986**, 34, 658.
17. Stul M. S.; Mortier W. J. *Clays Clay Miner.* **1974**, 23, 391.
18. Setton R. *Chemical Reactions In Organic and Inorganic Constrained Systems*, Nato Asi Series 165, D.; Reidel Publishing Co.: Dordrecht. 1986.
19. Freeman M. P. *J. Colloid. Interfac. Sci.* **1971**, 37, 760.
20. Vali H.; Kosier H. M. *Clay minerals* **1986**, 21, 827.
21. Solin S. A. *J. Mol. Catal.* **1984**, 27, 293.
22. Barrer R. M.; Brummer K. *Trans. Faraday Soc.* **1963**, 59, 959.
23. York B. R.; Solin S. A.; Wada N.; Raythatha R. H.; Johnson I. D.; Pinnavaia T. J. *Solid State Comm.* **1985**, 54, 475.
24. Foster M. D. *Clays Clay Miner.* **1961**, 10, 70.
25. Lee S.; Kim H.; Solin S. A.; Pinnavaia T. J., In *Chemical Physics of Intercalation*, Nato Asi Series Vol. 172; Legrand A. P.; Flandrois S. Eds.; Plenum Press: New York, 1987.
26. Dye J. L.; Nicely V. A. *J. Chem. Education* **1971**, 48, 443.

27. Hendricks S.; Teller E. *J. Chem. Phys.* **1942**, 10, 147.
28. Reynolds R.C. In *Crystal Structures of Clay Minerals and Their X-Ray Identification*; Brindley, G.W.; Brown, G., Eds.; Mineralogical Society: London, 1984; p 249.
29. Mathieson A. McL.; Walker G. F. *Am. Miner.* **1954**, 39, 231.
30. Wright A. C. *Clays Clay Miner.* **1973**, 21, 489.
31. Stout G.; Jensen L. H. *X-ray Structure Determination*; Macmillan Publishing Co., Inc.: New York, 1968.
32. Ishii J.; Shimanouchi T.; Nakamura M. *Inorganica Chemica Acta* **1967**, 1:3, 387.
33. Norrish K. J. *Colloid. Interface Sci.* **1975**, 50:1, 120.
34. Huong P.V.; Schlaak M. *Chem. Phys. Letters* **1974**, 27, 111.
35. Bertsch A. G.; Habgood H. W. *J. Phys. Chem.* **1963**, 67, 1621.
36. Howe R. F.; Taylor M.J. *Spectrochemica Acta* **1987**, 43, 77.
37. Fink D. H.; Nakayama F. S.; McNeal B. L. *Soil Sci. Soc. Amer. Pro.* **1971**, 35, 552.
38. McBride M. B.; Mortland M. M. *Clays Clay Miner.* **1973**, 21, 323.
39. Vansant E.F.; Uytterhoeven *Clays Clay Miner.* **1972**, 20, 47.
40. Davison N. *Statistical Mechanics*; McGraw Hill Book Co.: New York, 1962.

41. Xia W.; Thorpe M. F., *Phys. Rev. A* (to be published).

42. Reynolds R. C. *Clays Clay Miner.* **1986**, 34, 359.



MICHIGAN STATE UNIV. LIBRARIES



31293006066264